

Politecnico di Torino

Master of Science Degree in Mechanical Engineering

Academic Year 2024/2025

Graduation Session October 2025

Machine Learning-Based Derivation of a Mult-Variable Implicit Viscosity Model for Non-Newtonian Fluids

Supervisor: Author:

Prof. Daniela Misul Mohammad Amin Ghorbani

Co-Supervisor: Student ID:

Dr. **Bahram Haddadi** \$309719

Abstract

Viscosity, a fundamental rheological property of fluids, plays a key role in understanding and simulating flow behavior. This thesis presents a novel data-driven viscosity model for shear-thinning, time-independent non-Newtonian fluids, particularly elastomeric compounds processed in polymer manufacturing. The work begins with a detailed rheological characterization based on high-pressure capillary rheometry, employing Bagley and Weissenberg–Rabinowitsch corrections to extract accurate shear-stress and shear-rate data. Classical viscosity models, including the Carreau–Arrhenius formulation, were fitted using constrained nonlinear least squares to establish a physically meaningful baseline for augmented dataset generation.

To overcome experimental limitations in the low-shear region, the validated classical model was used to augment the dataset with 2000 synthetic data points. The enriched dataset enabled the development of the Multi-Variable Implicit (MVI) viscosity model, derived through symbolic regression using the PySR library. The MVI model yields a closed-form algebraic expression that implicitly couples temperature and shear rate without relying on exponential or logarithmic terms. This structure ensures compatibility with CFD solvers while maintaining smoothness, numerical stability, and high computational efficiency.

The model achieved an R² of 0.99 on unseen test data and demonstrated strong generalization across different polymer classes, including thermoplastics. It accurately reproduced the Newtonian plateau, transition region, and pseudoplastic regime. Although some non-Newtonian fluids exhibit a second Newtonian plateau at very high shear rates, the studied compound did not display such behavior within the experimentally accessible range. Consequently, the model was not trained on these extreme conditions and cannot capture that regime. The proposed approach bridges data-driven modeling and classical rheology, offering a viable path toward interpretable, AI-enhanced constitutive equations for engineering simulations.

Acknowledgements

This thesis marks the culmination of my Master's studies and would not have been possible without the support, guidance, and generosity of many individuals and institutions.

First and foremost, I would like to express my deepest gratitude to my supervisor, Professor **Daniela Misul**, and my co-supervisor, Dr. **Bahram Haddadi**, for their invaluable mentorship, technical insight, and constant encouragement throughout this project. Their guidance shaped every stage of this work and helped me grow both as a researcher and an engineer.

I am grateful to **TU Wien**, the **Competence Center CHASE GmbH**, and **SEMPERIT AG** for supporting this MSc thesis and making this academic–industrial collaboration possible. Special thanks to **Silke Koch** and **Florian Arthofer** from **SEMPERIT** for their support, and to the CHASE research scientists Dr. **Christian Marschik** and Dr. **Karin Wieland** for their expert input and thoughtful guidance during the thesis work.

A heartfelt thank you goes to Professor **Michael Harasek** (TU Wien) for his support and helpful discussions, which contributed greatly to the progress of this work.

I am also sincerely thankful to my colleague and friend **Mohammad Pourhosseinian**.

I am glad that this thesis became the beginning of our friendship, and I deeply appreciate the positive energy, teamwork, and motivation we shared during this journey.

Finally, I would like to express my deepest appreciation to my family for their unconditional love, patience, and encouragement. Their unwavering belief in me has been the foundation of my motivation and success throughout this journey.

This thesis is accompanied by a manuscript submitted to **Chemical Engineering Journal Advances** and a conference paper presented at the **20th OpenFOAM Conference, Vienna, 2025**. I thank everyone who helped shape the work that led to these contributions.

"This thesis was conducted within the COMET Centre CHASE, funded within the COMET – Competence Centers for Excellent Technologies programme by the BMIMI, the BMWET and the Federal Provinces of Upper Austria and Vienna. The COMET programme is managed by the Austrian Research Promotion Agency (FFG)."

List of Publications & Conference Papers

1. B. Haddadi, M.A. Ghorbani, C. Marschik, Pourhosseinian M. CFD," "Multi-Variable Non-Newtonian Viscosity Model in presented at the 20th OpenFOAM Conference, Vienna, Austria, 30 June – 4 July 2025.

[Conference Contribution]

 M. A. Ghorbani, M. Pourhosseinian, F. Arthofer, S. Koch, C. Marschik, D. Misul, B. Haddadi "Multi-Variable Implicit Viscosity Model for Shear-Thinning Fluids," submitted to Chemical Engineering Journal Advances, under review, July 2025.

[Journal Submission]

Table of Contents

Chapter 1 INTRODUCTION	.9
1.1 Literature Review	11
1.2 Problem Statement and Research Objectives	15
1.3 Structure of the Thesis	16
Chapter 2 Fundamentals of Non-Newtonian Fluid Rheology	18
2.1 Strain Rate Tensor Definition	19
2.2 Non-Newtonian Fluids	19
2.3 Rheological Regions in Shear-Thinning Fluids	20
2.4 Generalized Newtonian Fluids (GNF)2	21
2.5 Effect of Temperature and Static Pressure2	23
Chapter 3 Experimental Rheometry and Viscosity Correction Methods	24
3.1 Experimental Setup2	25
3.1.1 Cone-Plate Rheometry2	25
3.1.2 Capillary Rheometry2	26
3.1.3 Comparative Insights2	27
3.2 Apparent Viscosity2	29
3.3 Bagley Correction	31
3.4 Weissenberg-Rabinowitsch Correction	36
Chapter 4 Classical Viscosity Models for Shear-Thinning Fluids	40
4.1 Shear Rate-Dependent Viscosity Models	41
4.1.1 Power Law Model	41
4.1.2 Carreau Model	42
4.1.3 Cross Model	42
4.2 Temperature-Dependent Viscosity Models	43
4.2.1 Arrhanius Model	12

	44
4.2.3 Williams–Landel–Ferry (WLF) Equation	44
4.3 Combined Shear Rate and Temperature-Dependent Models	45
Chapter 5 Curve Fitting Methodology	47
5.1 Theoretical Basis of Nonlinear Least Squares	48
5.2 Iterative Numerical Solution	48
5.3 Practical Considerations in Viscosity Model Fitting	49
5.4 lmfit Python Library	50
5.5 Fit Results and Model Selection	50
Chapter 6 Data Preparation and Train-Test Partitioning	57
6.1 Limitations of Experimental Data	58
6.2 Synthetic Dataset Generation	58
6.3 Final Dataset Composition and Balancing	58
6.4 Train-Test Split Strategy	59
6.5 Final Preprocessing Steps	59
Chapter 7 Symbolic Regression	62
7.1 Introduction to Cymbolic Dograpsics	63
7.1 Introduction to Symbolic Regression	
7.1 Introduction to Symbolic Regression	
	64
7.2 Classical Methods in Symbolic Regression	64
7.2 Classical Methods in Symbolic Regression	64 64
7.2 Classical Methods in Symbolic Regression	64 64 65
7.2 Classical Methods in Symbolic Regression	64 65 66
7.2 Classical Methods in Symbolic Regression	
7.2 Classical Methods in Symbolic Regression	

7.5	Derived MVI Model Expression	71
7	7.5.1 Model Performance	72
Chapt	ter 8 Performance and Generalizability	74
8.1	Test Set Evaluation and Comparison with Classical Models	75
8.2	Evaluation on an Independent Dataset	80
Chapt	ter 9 Conclusion and Future Work	85
9.1	Conclusion	86
9.2	Limitations and Future Work	86
Biblio	graphygraphy	88

List of Figures

Figure 2.1) Rheological regions of the viscosity	21
Figure 3.1) An Overview of Cone-Plate Rheometer	26
Figure 3.2) Round die and Slit die configurations	27
Figure 3.3) Combined Rotational and Capillary techniques	28
Figure 3.4) Necessary Corrections by order based on die type	31
Figure 3.5) a) Newtonian Fluid b) Non-Newtonian Fluid	32
Figure 3.6) Linear Bagley correction plot	35
Figure 3.7) Shear stress corrected viscosity values	35
Figure 3.8) Shear rate corrected viscosity values	38
Figure 3.9) Corrected true viscosity data	39
Figure 5.1) Carreau-Arrhenius model fit results on corrected viscosity data. Shear Rate and Viscosity are in Logarithmic scale.	52
Figure 5.2) Extrapolation of Carreau-Arrhenius model fit results on corrected viscosity data. Shear Rate and Viscosity are in Logarithmic scale.	53
Figure 5.3) Carreau-Arrhenius model viscosity contour on final corrected viscosity	
Figure 5.4) Extrapolation of Carreau-Arrhenius model viscosity contour on final corrected viscosity data	55
Figure 6.1) A sample of final synthetic data set	61
Figure 7.1) Tree-Shaped symbolic regression algorithm structure	64
Figure 7.2) a)Mutation applied to the expression tree. b) Crossover applied to two	69
Figure 8.1) Carreau-Arrhenius fit results on the test set	75
Figure 8.2) MVI Model fit results on the test set	76
Figure 8.3) Extrapolation of Carreau-Arrhenius model on the test set	76

Figure 8.4) Extrapolation of MVI model on the test set
Figure 8.5) a) Carreau-Arrhenius viscosity contour on the test set. b) MVI Viscosity
model viscosity contour on the test set
Figure 8.6) a) Carreau-Arrhenius model extrapolation of the viscosity contour on the
test set. b) MVI Viscosity model extrapolation of the viscosity contour on the test set.
79
Figure 8.7) Viscosity measurements of independent validation datasets under varying
shear rates and temperatures: a) Polypropylene (PP) b) Polystyrene (PS)
c)Acrylonitrile Butadiene Styrene (ABS). The plot is in logarithmic scale82
Figure 8.8) Fit results of the MVI viscosity model on independent validation datasets:
a) Polypropylene (PP) b) Polystyrene (PS) c) Acrylonitrile-Butadiene-Styrene (ABS)83

List of Tables

Table 4-1) Multi-Variable constitutive viscosity models	. 46
Table 5-1) Extracted fit parameters of Carreau-Arrhenius model from the corrected	ŀ
dataset	. 55
Table 7-1) Physical interpretation of MVI model parameters	.72
Table 8-1) Derived variables of Carreau-Arrhenius viscosity model	. 80
Table 8-2) Derived variables of MVI viscosity model.	. 80
Table 8-3) Fit statistics of MVI viscosity model un independent dataset	83

Chapter 1 | INTRODUCTION

Understanding the behavior of fluids is essential for designing and optimizing processes in industries ranging from polymer processing and additive manufacturing to biomedical devices and energy systems [1], [2]. At the core of rheology is viscosity, which describes how a fluid resists deformation. For simple fluids like water or air, viscosity remains constant regardless of how fast the fluid is being sheared. These are known as Newtonian fluids, and their shear stress and shear rate relationship follows a linear law [3]. However, many real-world fluids behave quite differently. Their viscosity can change depending on the shear rate, temperature, or even time. These are called non-Newtonian fluids [4]. A particularly important subclass is shear-thinning or pseudoplastic fluids. These materials, which include polymer melts, slurries, and biological fluids, become less viscous as they are sheared more [5].

The ability to predict and control the viscosity of such fluids is of great practical importance. In polymer processing, for instance, the viscosity determines how easily materials flow through dies and molds, directly influencing product quality, dimensional stability, and energy consumption. Similarly, in biomedical and energy systems, precise viscosity modeling governs the accuracy of simulations involving blood flow, lubrication, and heat transfer. In these contexts, even small modeling inaccuracies can propagate through computational frameworks, leading to significant errors in predicted flow behavior or system performance.

Over the decades, numerous constitutive models have been developed to describe viscosity as a function of shear rate or temperature. Classical models such as the Power Law, Carreau, and Cross formulations have proven effective in characterizing shear-dependent behavior, while Arrhenius or WLF equations capture thermal effects. However, these models typically treat the two effects independently, which limits their applicability under conditions where shear rate and temperature interact strongly, as in non-isothermal polymer flows. When these equations are combined to capture both effects at the same time, they lead to mathematically complex expressions that are difficult to calibrate and computationally expensive to implement in CFD solvers.

In recent years, Artificial Intelligence (AI) and Machine Learning (ML) techniques have been increasingly employed to overcome the nonlinear and coupled nature of these dependencies. While these data-driven approaches demonstrate high predictive accuracy, they often sacrifice physical interpretability and introduce computational overhead, making them less suitable for integration into industrial simulation workflows. This motivates the need for a new modeling framework that preserves the interpretability and simplicity of classical rheological models while leveraging the flexibility of data-driven discovery. The present thesis addresses this need by developing a unified, compact, and physically interpretable viscosity model capable of representing the coupled influence of shear rate and temperature efficiently.

1.1 Literature Review

In polymer processing, the shear-thinning behavior is crucial. When polymers are extruded or injected into molds, the reduction in viscosity under high shear allows smoother and more efficient flow [6]. Shear-thinning behavior is commonly described using mathematical models such as Carreau, Cross, and Power Law formulations. Among these, the Carreau model and its extension, Carreau-Yasuda model are particularly popular due to their ability to represent both the low and high shear rate Newtonian plateaus. Their capability to accurately capture the transition between these regions makes it especially suitable for complex flow scenarios, including hydraulic fracturing and flow over deformable boundaries [7], [8], [9]. Compared to simpler formulations such as the Power Law, the Carreau family of models provides a more robust framework for simulating shear-thinning fluids, effectively balancing physical accuracy with numerical stability in high-fidelity CFD simulations [10].

The Cross model is a well-known constitutive equation for describing shear-thinning fluids. It's often used in blood flow simulations, where it helps predict how shear stress and velocity change across the aorta [11]. Compared to the Carreau model, the Cross model is simpler and easier to work with, which makes it a popular choice, especially in the polymer industry. It works well for fluids that act like Newtonian fluids at low shear rates but become shear-thinning as the shear rate increases [12].

The Power Law model remains one of the most frequently applied formulations for describing the flow behavior of non-Newtonian fluids, particularly those exhibiting shear-thinning or shear-thickening characteristics. Its widespread use stems largely from its mathematical simplicity, having only two fit parameters. This makes it especially appealing for integration into both analytical frameworks and computational tools, where it facilitates rapid estimation of viscosity across different shear rates. In practical terms, the Power Law model performs well in polymer processing operations such as extrusion and molding, where materials are subjected to a broad range of shear rates and rapid viscosity changes are expected [13]. However, a critical limitation of the Power Law model is its inability to represent the Newtonian behavior at very low and very high shear rates. It assumes a continuous power-law relationship throughout, which leads to unrealistic predictions. For

example, it suggests that viscosity becomes infinite as the shear rate approaches zero [14]. This is not only physically inaccurate but also introduces numerical instability in CFD simulations, particularly when modeling flow start-up or near-stagnant regions [15].

While these models focus primarily on the effect of shear rate, viscosity is also strongly influenced by temperature, especially in thermally sensitive or non-isothermal processes. As the temperature rises, the enhanced molecular mobility within the fluid reduces its viscosity, introducing a nonlinear behavior in the viscosity relationship. This nonlinearity must be captured carefully in simulations to avoid inaccurate flow predictions, particularly in applications like extrusion, injection molding, or lubrication, where temperature gradients are substantial and directly affect performance.

One of the most widely used models for representing this temperature-viscosity relationship is the Arrhenius equation. This model assumes an exponential decay of viscosity with temperature, based on the idea that increased thermal energy helps molecules overcome intermolecular resistance more easily. The strength of the Arrhenius model lies in its simplicity: it requires only a few parameters including the activation energy, the universal gas constant, and a pre-exponential factor, which makes it computationally lightweight and easy to implement in both experimental analysis and CFD codes. Its analytical form also allows for convenient curve fitting and extrapolation within moderate temperature ranges [16].

However, the Arrhenius equation becomes less reliable near the glass transition temperature (T_g) of polymeric or amorphous materials. In these regions, the physical behavior of the fluid deviates from the assumptions underpinning the Arrhenius model. Instead of following a smooth exponential trend, the viscosity tends to change more abruptly, reflecting the complex structural relaxation processes taking place within the material matrix. This deviation significantly impacts simulation accuracy when modeling temperature-sensitive systems or when temperature variations bring the material close to T_g .

To address these limitations, more sophisticated semiempirical models such as the Williams-Landel-Ferry (WLF) and Vogel–Fulcher–Tammann (VFT) equations have been introduced. These models are specifically designed to better capture the non-Arrhenius behavior of fluids near T_g . The WLF model, for instance, is derived from polymer relaxation theory and is widely applied in time-temperature superposition techniques. It expresses the logarithmic shift in viscosity as a function of temperature relative to Tg, offering a more accurate prediction in the vicinity of this critical threshold. Similarly, the VFT model modifies the simple exponential structure of the Arrhenius equation by introducing a temperature offset, which reflects the asymptotic slowing down of molecular motion as temperature decreases toward the material's glassy state [17].

While classical viscosity models have played a fundamental role in understanding fluid behavior, they typically handle only one influencing factor at a time, either shear rate or temperature. However, in real-world scenarios, especially in complex industrial processes, both of these variables simultaneously affect the viscosity of non-Newtonian fluids. Shear-thinning fluids, for instance, not only change their viscosity with flow but also respond sensitively to thermal conditions. To account for this, researchers have often combined a shear rate-dependent model like Carreau or Power Law with a temperature-dependent formulation such as the Arrhenius or WLF model. Although this coupling improves predictive accuracy, it results in complex and highly nonlinear equations that are difficult to implement efficiently in computational environments such as CFD solvers. These equations require careful calibration and often become computationally expensive.

To address this challenge, the scientific community has increasingly explored Artificial Intelligence (AI) and Machine Learning (ML) techniques as alternative approaches for modeling viscosity. These data-driven methods offer a powerful way to capture nonlinear relationships. One notable example is the work by Daniel R. Cassar, who applied a Neural Network framework to estimate the temperature-dependent viscosity by predicting the fitting parameters of the MYEGA equation. His approach demonstrated that neural networks could successfully replicate established

empirical laws with minimal human intervention, thereby streamlining the model generation process [18].

Further studies have extended this idea by using more advanced neural network architecture. For instance, in the work by D. Li et. Al., Multilayer Perceptron Neural Networks (MLPs) and Decision Trees have been implemented to predict the viscosity of crude oil. These models have achieved high predictive accuracy, often outperforming traditional regression-based techniques. Their ability to capture complex, high-dimensional relationships make them particularly well-suited for modeling fluids with nonlinear behavior under varying flow and thermal conditions [19].

In another relevant study, A.M. Elsharkwy et al. compared Classical Regression Techniques (CRT) and Neural Regression Techniques (NRT) for viscosity prediction. Their results revealed that NRTs were significantly more accurate, especially when dealing with highly nonlinear data. This emphasized the potential of machine learning not just as a supplement, but as a viable replacement for traditional empirical models in certain scenarios [20].

Moreover, Artificial Neural Networks (ANNs) have also been successfully employed to predict the viscosity of black oil below its bubble point. This application is particularly complex due to phase changes and strong pressure dependencies, yet the ANN model delivered better predictive performance than previously introduced physical models [21]. Similarly, researchers like Y. Hajizadeh explored hybrid AI techniques that combined Fuzzy Logic with Neural Networks. Their work showed that integrating rule-based inference systems with machine learning could further enhance accuracy, especially when dealing with sparse or noisy datasets [22].

Perhaps one of the most promising developments in this space is the work by Saadat et al., who introduced a Rheology-Informed Neural Network (RhINN) framework. Unlike conventional machine learning models that act as black boxes, RhINNs embed physical constraints into the learning process. In their study, the neural network was trained to select the most appropriate constitutive model out of nine candidates by evaluating how well each model fits a given shear rate dataset. This combination of

domain knowledge and machine learning flexibility enabled the algorithm to autonomously identify the best-fit model [23].

Despite the success of these AI-based methods, challenges remain. Many of these models require large amounts of high-quality data for training, and they often need to be re-trained for each new fluid or set of conditions. Additionally, their complexity can introduce integration barriers in computational simulations, especially where real-time performance or memory efficiency is critical. Therefore, the development of a simpler yet accurate modeling strategy remains crucial for bridging the gap between predictive performance and computational efficiency in rheological modeling.

1.2 Problem Statement and Research Objectives

Despite significant advances in rheological modeling, accurately representing the viscosity of shear-thinning fluids under coupled shear-rate and temperature variations remains an open challenge. Classical viscosity models, while physically grounded, require composite formulations to account for both shear-dependent and thermal behavior. These compound models introduce mathematical nonlinearity and parameter redundancy, which can severely impact computational efficiency and stability when implemented in finite volume or finite element solvers. Furthermore, many of these formulations rely on exponential terms or piecewise definitions, complicating their integration into industrial CFD frameworks.

On the other hand, artificial intelligence and data-driven approaches have shown strong predictive power but lack interpretability and often demand significant training data and computational resources. Their complexity makes them impractical for fast simulations or real-time control systems, where stability, speed, and transparency are critical.

In this context, the main research problem addressed by this thesis is the development of a unified, compact, and physically interpretable viscosity model that accurately captures the coupled influence of shear rate and temperature without the overhead of traditional or purely data-driven approaches.

The specific research objectives are:

- To formulate a new viscosity model that inherently accounts for the nonlinear interaction between shear rate and temperature using a single, closed-form expression.
- To reduce the computational complexity of existing models while preserving or improving accuracy, by deriving a mathematically efficient structure suitable for direct implementation in CFD solvers.
- To employ symbolic regression as the core modeling tool, enabling automatic discovery of closed-form equations from experimental and synthetic data.
- To evaluate the proposed MVI model against traditional models such as Carreau-Arrhenius in terms of predictive accuracy.

1.3 Structure of the Thesis

Due to the hierarchical structure and method-development focus of this thesis, the results are presented within each relevant chapter and section. This integrated approach reflects the sequential nature of the work, where the outcome of each stage serves as a necessary foundation for the subsequent one.

The remainder of the thesis is organized as follows:

- Chapter 2 provides the theoretical foundation for non-Newtonian fluid rheology. It introduces the strain rate tensor, classifies non-Newtonian and generalized Newtonian fluids, and discusses the influence of pressure and temperature on viscosity, as well as typical viscosity regions in shear-thinning behavior.
- Chapter 3 presents rheometry techniques relevant to this study, comparing high-pressure capillary rheometers and cone-and-plate devices. It also details correction methods, including Bagley and Weissenberg–Rabinowitsch corrections, to ensure accurate viscosity measurements.
- Chapter 4 reviews classical viscosity models, separating shear ratedependent and temperature-dependent formulations. It also discusses combined multi-variable models and evaluates their strengths and limitations in capturing complex rheological behavior.

- Chapter 5 outlines the curve fitting methodology used to calibrate viscosity models. It introduces the theory of nonlinear least squares minimization, describes numerical solution methods, and presents the lmfit implementation with constraints reflecting physical bounds.
- Chapter 6 describes the data preparation strategy, including the limitations of experimental data, generation of synthetic data using Carreau–Arrhenius models, and final dataset assembly. It also defines the train–test split and preprocessing pipeline used prior to symbolic regression.
- Chapter 7 introduces symbolic regression as a model discovery tool, discusses classical and modern approaches, formalizes the learning problem, and presents the PySR framework used to derive the final MVI model through multi-objective optimization.
- Chapter 8 evaluates the performance and generalizability of the MVI model. Its accuracy is assessed on test data and additional compound datasets, highlighting its robustness, generalization capability, and suitability for CFD integration.
- Chapter 9 concludes the thesis by summarizing the key contributions, discussing the advantages and potential limitations of the MVI model, and suggesting directions for future research and CFD integration.

References are provided at the end of the thesis for reproducibility and transparency.

Chapter 2 | Fundamentals of Non-Newtonian Fluid Rheology

This chapter establishes the theoretical and mathematical framework underlying the rheological modeling used in this study, with particular focus on shear-thinning polymeric fluids. The fundamental equations and tensor definitions presented here are primarily based on Irgens [24] and provide the background necessary for formulating constitutive relationships later applied in model development and simulation.

The chapter begins by defining essential quantities such as the rate-of-strain tensor and the shear rate. It then proceeds to classify Newtonian and non-Newtonian fluids, discusses generalized Newtonian formulations, and examines how pressure and temperature influence viscosity. In addition, it presents the characteristic rheological regions typically observed in a viscosity-shear-rate curve, including the low-shear Newtonian plateau, the intermediate transition region, and the high-shear thinning regime. The physical significance of these regions and their relevance to polymer-processing applications are emphasized, as they form part of the theoretical foundation for the modeling, data generation, and symbolic-regression analyses developed in the later chapters.

2.1 Strain Rate Tensor Definition

For incompressible flows, the rate-of-strain tensor D is defined as the symmetric part of the velocity gradient tensor:

$$D = \frac{1}{2}(\nabla u + (\nabla u)^t)$$
 (2-1)

where u is the velocity vector. This tensor quantifies the rate at which fluid elements deform. From D, the scalar shear rate $\dot{\gamma}$ is often defined as the second invariant:

$$\dot{\gamma} = \sqrt{2tr(D^2)} \tag{2-2}$$

Where tr(-) is the trace operator. This shear rate serves as the primary input in generalized Newtonian models, describing the dependence of viscosity on the flow field.

2.2 Non-Newtonian Fluids

Unlike Newtonian fluids where viscosity remains constant, non-Newtonian fluids exhibit a viscosity that depends on shear rate, time, temperature, or stress history. Based on the dependency, non-Newtonian fluids are broadly classified into [24]:

- **Time-independent fluids**: In these fluids, viscosity depends only on the instantaneous shear rate, and they can be categorized to pseudoplastic (shearthinning), dilatant (shear-thickening), and Bingham-type materials.
- **Time-dependent fluids**: Viscosity changes over time under constant shear. Examples include thixotropic fluids (viscosity decreases with time) and rheopectic fluids (viscosity increases with time).
- **Viscoelastic fluids**: These display both elastic and viscous behavior. Under stress, they initially deform elastically and then flow like a viscous fluid. These fluids require more complex constitutive equations involving relaxation and retardation times.

This study focuses on shear-thinning, time-independent fluids, particularly elastomer compounds with no significant yield stress or time-dependent effects under the investigated conditions.

2.3 Rheological Regions in Shear-Thinning Fluids

Shear-thinning materials exhibit distinct flow regimes as a function of shear rate. A typical viscosity–shear rate curve, plotted on logarithmic axes, can be segmented into the following key regions:

Newtonian Plateau (Zero-Shear Viscosity Region):

At very low shear rates, the viscosity remains approximately constant. This is referred to as the zero-shear viscosity, η_0 , and characterizes the fluid's resistance to flow in the absence of significant deformation. Molecular chains or internal microstructures are in a relaxed, entangled state.

Transition Region:

As the shear rate increases, polymer chains or suspended structures begin to align and disentangle in the direction of flow. This leads to a rapid decrease in viscosity and the breakdown of the Newtonian assumption. This nonlinear zone connects the Newtonian plateau with the shear-thinning region and varies in width depending on the fluid's microstructure and temperature.

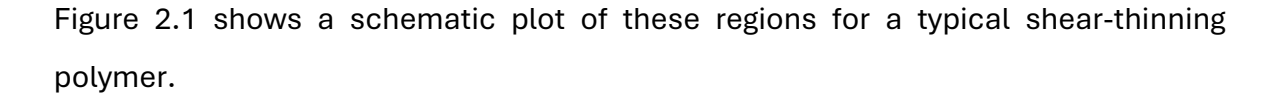
Shear-Thinning (Pseudoplastic) Region:

At moderate to high shear rates, the fluid shows a nearly linear behavior in log–log space.

Here, molecular alignment reduces internal friction, leading to a continued decline in viscosity with an increasing shear rate. This region dominates industrial processing operations such as extrusion, injection molding, or mixing.

Second Newtonian Plateau:

In some complex polymer melts or structured fluids, viscosity may stabilize again at extremely high shear rates due to complete alignment of molecular chains. This second Newtonian plateau is difficult to capture experimentally and was not observed in the current study.



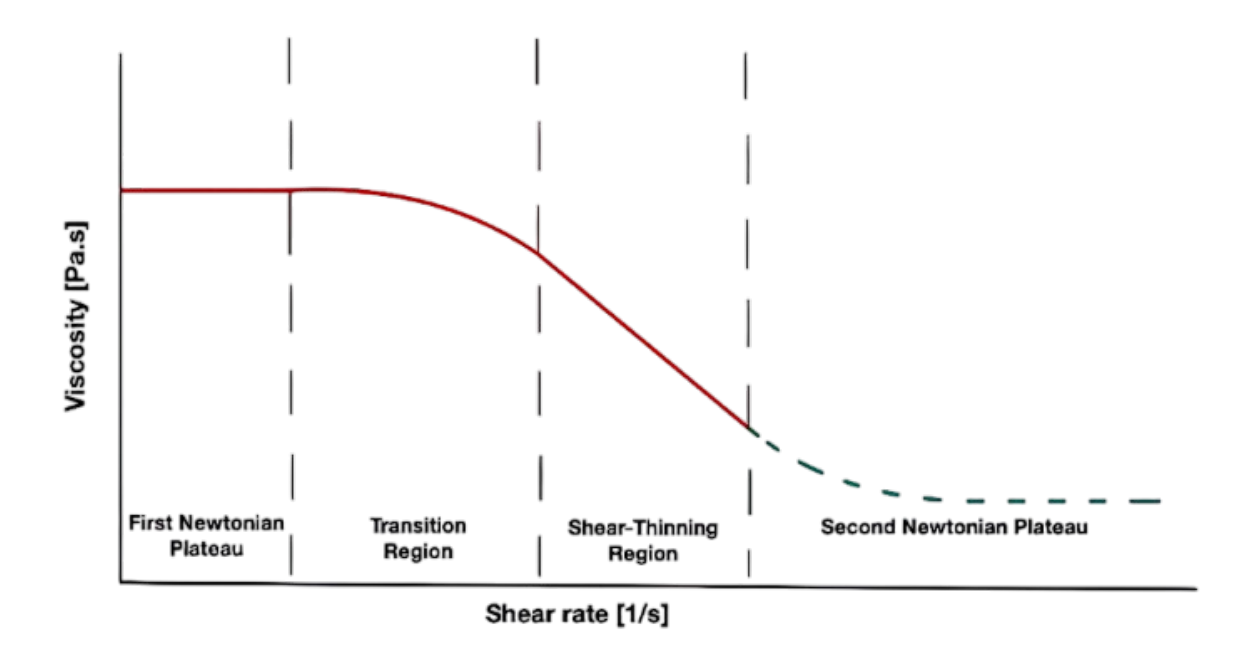


Figure 2.1) Rheological regions of the viscosity

2.4 Generalized Newtonian Fluids (GNF)

Generalized Newtonian Fluids are a class of time-independent non-Newtonian fluids where the extra stress tensor is defined as:

$$T' = 2\eta_{(\dot{\gamma})}D \tag{2-3}$$

Here, $\eta_{(\dot{\gamma})}$ is the apparent viscosity, a scalar function of the shear rate $\dot{\gamma}$. This framework retains the structure of the Newtonian model but generalizes it by allowing viscosity to vary with flow conditions.

Common models used to define $\eta_{(\dot{\gamma})}$ include:

Power Law: This model is considered as one of the simplest and most straightforward viscosity models, while suffering from limitations in first and second Newtonian plateaus.

$$\eta_{(\dot{\gamma})} = K \cdot \dot{\gamma}^{n-1} \tag{2-4}$$

Spriggs Model: A truncated Power Law that limits η for 0 shear rate in order to prevent the model from predicting infinite value for viscosity and reads as:

$$\eta_{(\dot{\gamma})} = \eta_0 \quad if \quad \dot{\gamma} \le \dot{\gamma}_0 \quad , \quad \eta_{(\dot{\gamma})} = \eta_0 (\frac{\dot{\gamma}}{\dot{\gamma}_0})^{n-1} \quad if \quad \dot{\gamma} > \dot{\gamma}_0$$
(2-5)

Cross Model: A shear rate dependency model that captures Newtonian plateau by incorporating a zero-shear viscosity parameter, avoiding the viscosity to reach infinity at zero shear rate.

$$\eta_{(\dot{\gamma})} = \frac{\eta_0}{1 + \left(\frac{\eta_0 \cdot \dot{\gamma}}{\tau^*}\right)^{1-n}} \tag{2-6}$$

Carreau Model: This model also handles zero shear viscosity and is widely used to describe viscosity behavior of polymers.

$$\eta_{(\dot{\gamma})} = \eta_0 \cdot (1 + (\lambda \dot{\gamma})^2)^{\frac{(n-1)}{2}}$$
(2-7)

Bingham Model: Includes a yield stress τ_0 and a linear post-yield flow and defined as:

$$\eta_{(\dot{\gamma})} = \mu + \frac{\tau_y}{\dot{\gamma}} \quad \text{when} \quad \tau_{max} \ge \tau_y \quad \text{and} \quad \eta_{(\dot{\gamma})} = \infty \quad \text{when} \quad \tau_{max} < \tau_y \quad (2-8)$$

Herschel–Bulkley / Ellis Models: Combine shear-thinning and yield stress behavior, defined as:

$$\eta_{(\dot{\gamma})} = \frac{\tau_0}{\dot{\gamma}} + K \dot{\gamma}^{n-1} \tag{2-9}$$

These models are widely implemented in computational fluid dynamics (CFD) and are crucial for accurate prediction of flow in polymer processing. As the aim of the present study is focused on the behavior of shear-thinning fluids, a more complete explanation of models capable of describing such behavior will be given in **Chapter 4**.

2.5 Effect of Temperature and Static Pressure

Viscosity is highly temperature-dependent. Several models are used to capture this effect:

Arrhenius Law:

$$\eta_{(T)} = \eta_a \cdot e^{\left(\frac{E_a}{R \cdot T}\right)} \tag{2-10}$$

Williams-Landel-Ferry (WLF) Law:

$$\eta_{(T)} = \eta_0 \cdot e^{\left(-\frac{C_1 \cdot (T - T_g)}{C_2 + (T - T_g)}\right)}$$
(2-11)

Vogel-Fulcher-Tammann (VFT):

$$\eta_{(T)} = \eta_0 \cdot e^{\left(\frac{E_0}{R \cdot (T - T_0)}\right)}$$
(2-12)

The VFT equation can be viewed as an Arrhenius-type model with a shifted reference temperature, making their functional forms qualitatively similar under certain parameterizations. A more detailed comparison between temperature dependency models is given in **Chapter 4**.

Pressure also affects viscosity, but to a lesser extent. For polymers, a 1000-bar increase in pressure can have an effect similar to a 15–30 °C temperature change on the shear viscosity [25]. In this study, due to equipment limitations and negligible effects of the pressure on viscosity, pressure-dependent effects are disregarded.

Chapter 3 | Experimental Rheometry and Viscosity Correction Methods

This chapter presents the experimental framework used to obtain viscosity data for the development of the proposed model. The measurements were conducted using a high-pressure capillary rheometer, which is particularly suited for characterizing polymeric fluids under high-shear, processing-relevant conditions. This technique enables the accurate determination of shear-dependent viscosity across the range most representative of industrial flows.

In addition to describing the experimental setup, the chapter outlines the correction procedures necessary to convert raw measurements into true rheological quantities. The Bagley and Weissenberg–Rabinowitsch corrections are applied sequentially to eliminate entrance losses and account for non-Newtonian velocity profiles, respectively. The corrected viscosity dataset obtained from these experiments serves as the foundation for the model calibration and validation stages discussed in subsequent chapters.

3.1 Experimental Setup

Various types of rheometers have been developed to measure viscosity under different shear conditions. This study primarily utilized capillary rheometry, which is well-suited for high-shear industrial conditions [26]. For completeness, a brief overview of coneplate rheometry, commonly employed for low-shear oscillatory measurements in laboratory settings is also included [27]. Each method provides distinct yet complementary insights into the flow behavior of shear-thinning materials.

3.1.1 Cone-Plate Rheometry

In the cone-plate configuration, the sample is placed between a flat plate and a shallow-angle cone, which rotates to impose shear. In the case of parallel-plate geometry, two flat, circular plates are used instead, with the upper plate rotating at a specified angular velocity. In fact, the fluid is sheared between a stationary and moving wall. The fluid is adhered to the moving wall and dragged along it [28].

Cone-plate rheometry is particularly useful in the low shear rate domain where capillary rheometers may lack resolution or produce unstable data due to limitations such as pressure sensor range and entrance effects. However, cone-plate rheometry has its own challenges, including potential edge fracture, slippage at the wall, and sample drying or degradation during extended high-temperature measurements. Figure 3.1 illustrates an overview of cone-plate rheometer structure [29].

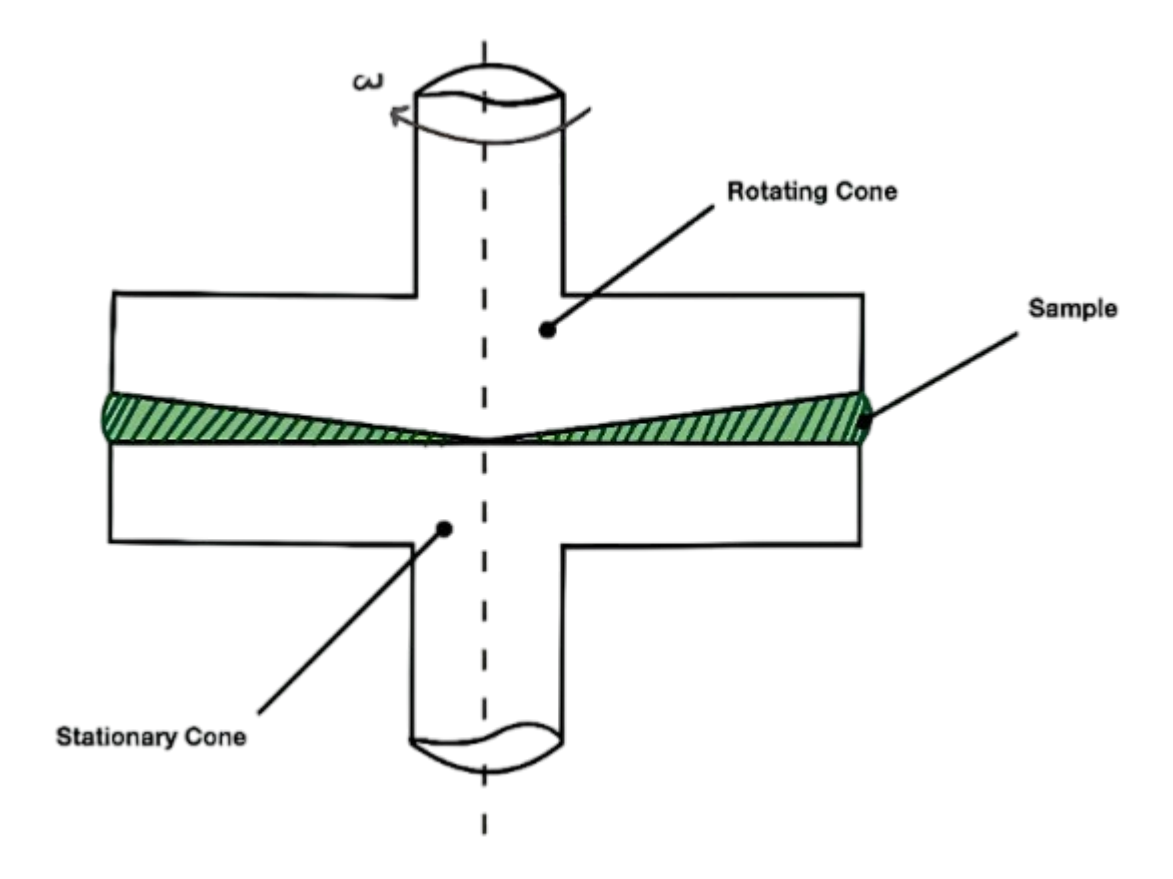


Figure 3.1) An Overview of Cone-Plate Rheometer.

3.1.2 Capillary Rheometry

Capillary rheometry, and specifically high-pressure capillary rheometry, represents a powerful approach for characterizing fluid viscosity under high-shear conditions. The principle behind high-pressure capillary rheometers involves pushing the sample through a cylindrical or slit-shaped channel using a piston, generating a pressure-driven flow [30]. These devices are generally classified into two types: Speed Control and Pressure Control systems [31]. In this work, a Speed Control rheometer with round channel was used, where the piston sets the flow rate while pressure data is recorded. Once the pressure curve stabilizes, a measurement point is taken, after which the piston speed is increased to reach the next shear rate. The experiments were conducted and provided by **SEMPERIT AG** using a **Rheograph 25/50 (Göttfert GmbH)**, with test temperatures ranging from 70 °C to 120 °C and shear rates from approximately 10 s⁻¹ to 5000 s⁻¹. These conditions align with the recommended operational window for such instruments [32].

The material tested had a glass transition temperature around –50 °C. The main die used in the tests was 20 mm long with a 2 mm diameter, corresponding to a 10:1 aspect ratio. As illustrated in Figure 3.2, pressure sensors in round dies can only be installed at the die entrance, which limits direct measurement of the pressure drop along the channel [33]. In addition to the primary die, a secondary short die of 0.2 mm length, used for Bagley correction. This arrangement enables linear Bagley correction to be applied, compensating for entrance pressure losses that are otherwise inseparable from pressure drop along the die.

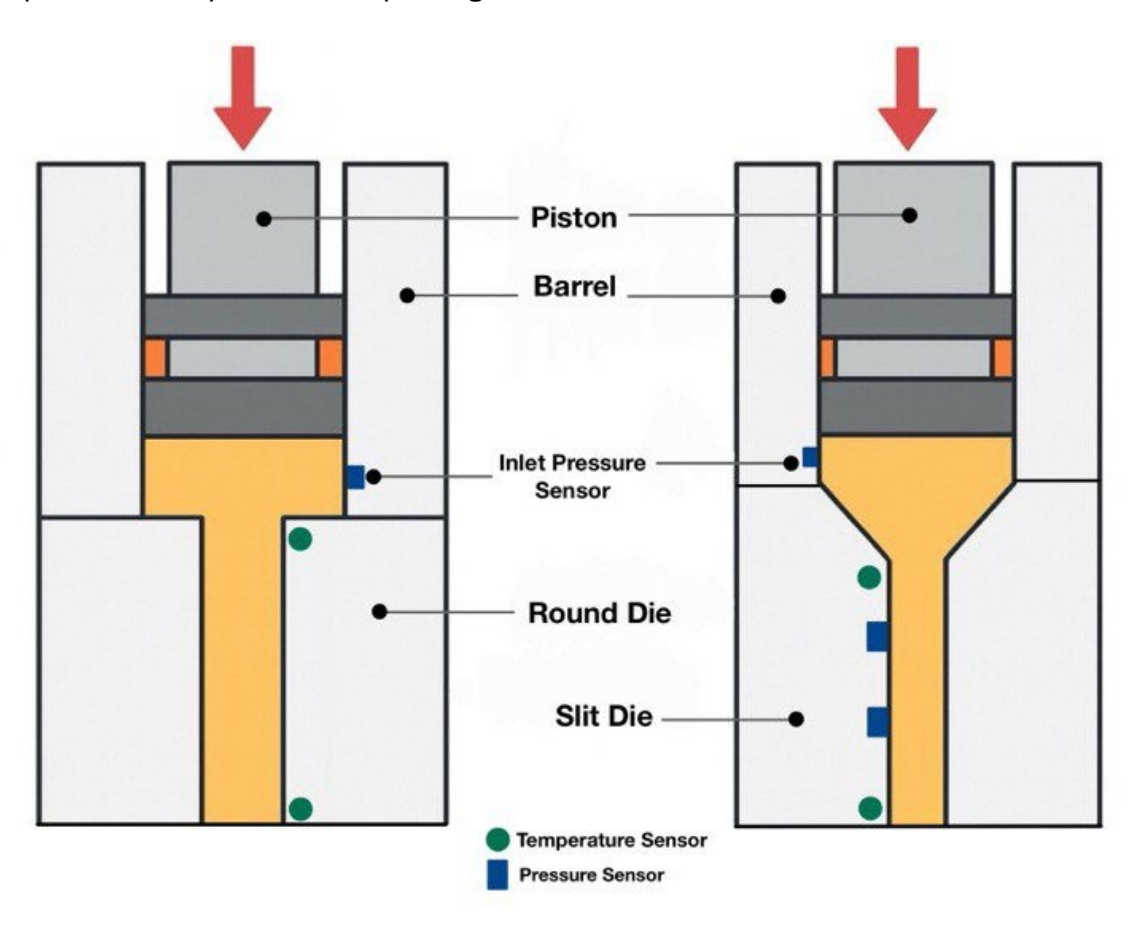


Figure 3.2) Round die and Slit die configurations

3.1.3 Comparative Insights

While both rheometry techniques aim to characterize shear-dependent viscosity, they differ significantly in their measurement regimes and associated assumptions. Coneplate rheometry is best suited for low to moderate shear rates and is ideal for capturing

viscoelastic properties and linear viscoelastic spectra under oscillatory conditions. However, it lacks the ability to replicate the high-shear environments experienced in real-world processes like extrusion.

In contrast, capillary rheometry provides access to high shear rates, capturing the shear-thinning behavior and temperature dependence under pressure-driven flow, closely mimicking processing conditions in polymer extrusion, molding, and compound shaping.

Considering the advantages of both techniques, it's best to combine these methods to achieve a reliable and broad range of viscosity data as illustrated in Figure 3.3. The reason behind it is at low shear rates, torque and pressure is low, therefore cone-plate rheometer is the best option. However, in high shear rates, torque and pressure increases which results in flow instability. In this regime, capillary rheometry is the best option.

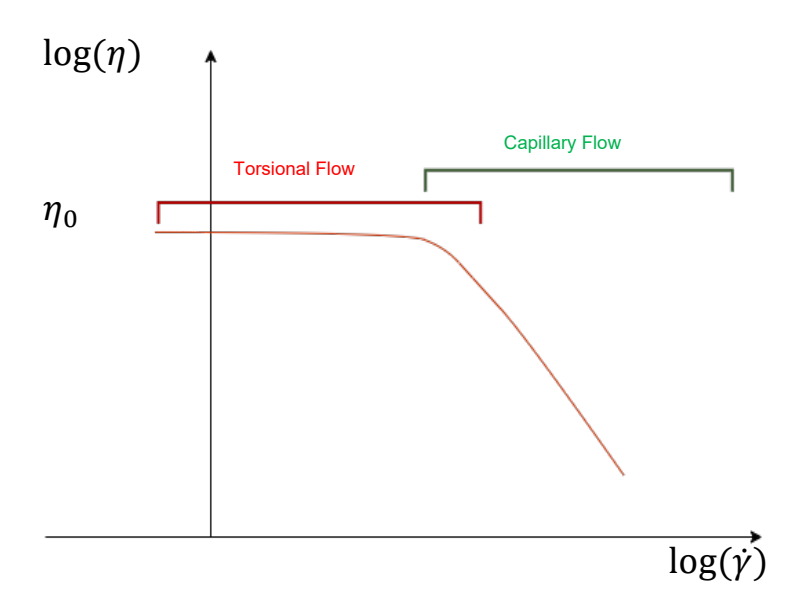


Figure 3.3) Combined Rotational and Capillary techniques

In this study, the capillary rheometer was used to build the primary dataset for model development, due to its ability to cover the shear rate domain of industrial interest.

3.2 Apparent Viscosity

Measuring viscosity through rheometry techniques involves several assumptions during the experimental measurement. Consequently, the viscosity values obtained through such techniques do not represent the true behavior of the fluid unless we account for these assumptions and errors. Therefore, the concept of Apparent Viscosity is introduced, which means the measured viscosity does not actually represent the true behavior of the fluid, and appropriate correction procedures must be applied to obtain true viscosity values, depending on the material, rheometry technique, and the device used for measurements.

The need for correction depends primarily on two factors: (1) the flow channel geometry of the rheometer (round vs. slit die), and (2) the rheological behavior of the fluid, particularly whether it exhibits high viscosity and elastic behavior or behaves more like a Newtonian or mildly shear-thinning fluid.

For highly viscous materials, such as polymer melts or elastomers, the following correction sequence is typically required to achieve accurate viscosity values:

- Bagley correction: to account for entrance pressure losses that are significant due to the material's resistance to deformation,
- Dissipation correction: to account for heating effects caused by internal viscous dissipation,
- Mooney correction: for wall slip in cases of highly elastic melts,
- Weissenberg-Rabinowitsch correction: to convert apparent shear rate to true shear rate.

In contrast, for low-viscosity fluids, such as dilute solutions or oils, the correction sequence differs:

- Hagenbach correction: accounts for kinetic energy effects (non-viscous losses) in capillary viscometry,
- Bagley correction: compensates for entrance effects,

Weissenberg–Rabinowitsch correction: accounts for shear-thinning effects,
 non-parabolic velocity profile and corrects the shear rate.

Moreover, the correction order is influenced by the geometry of the capillary die:

- In round dies, pressure is typically measured only at the entrance, making Bagley correction essential to isolate pressure drops caused by fully developed flow.
- In slit dies, pressure can be measured along the channel, potentially allowing direct estimation of shear stress, thereby influencing which corrections are applied and in what sequence.

These considerations highlight that no single correction protocol fits all scenarios. we must select and apply the appropriate corrections based on the specific flow configuration and fluid rheology. In the current study, since we are dealing with highly viscous, shear-thinning polymeric fluids using round capillary dies, we follow the established order of applying Bagley correction first to obtain true shear stress, followed by the Weissenberg–Rabinowitsch correction to calculate true shear rate. This sequential correction ensures accurate determination of true shear viscosity [34]. Figure 3.4 shows the sequence of applying the two most important corrections based on die type used.

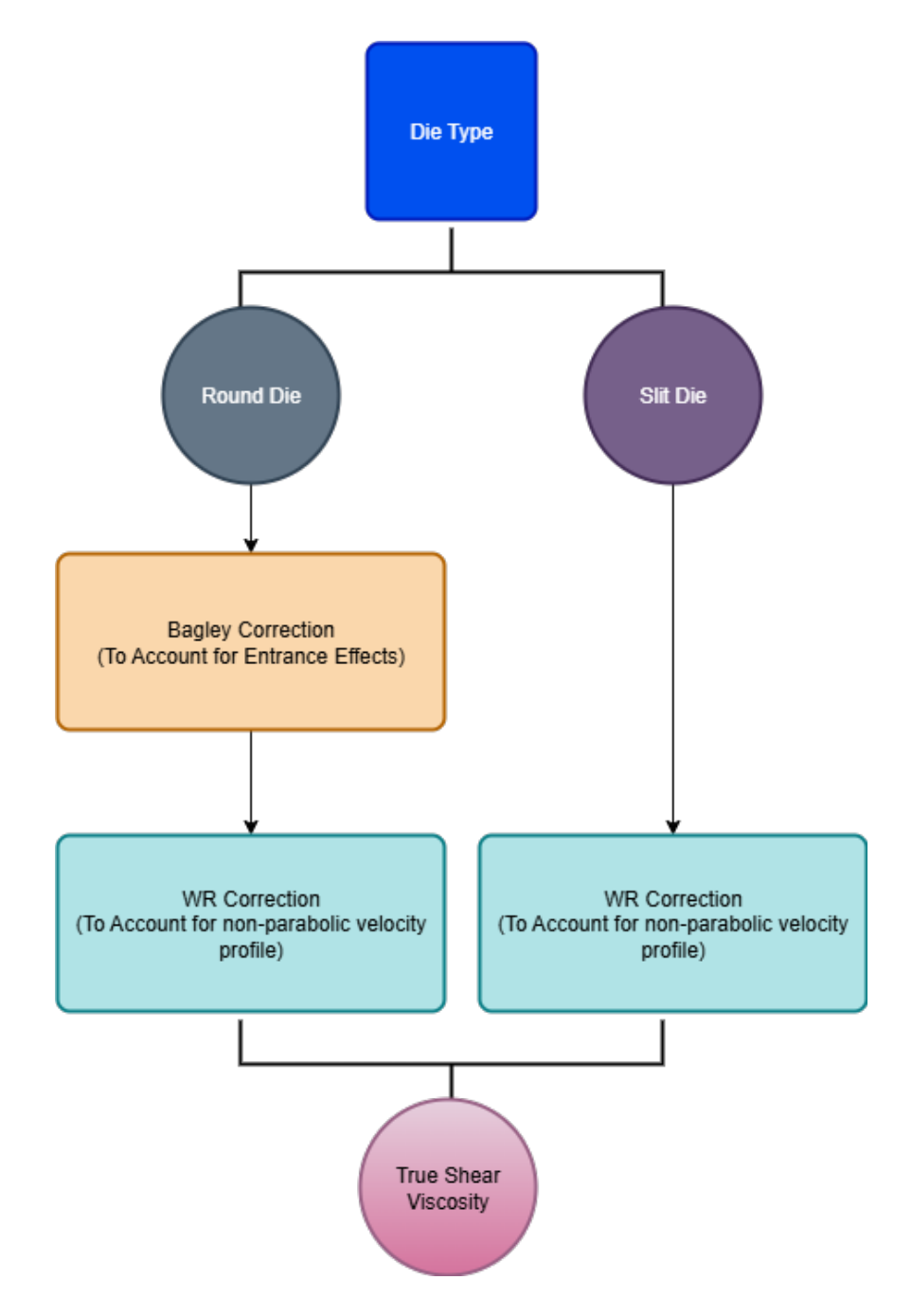


Figure 3.4) Necessary Corrections by order based on die type

3.3 Bagley Correction

In high-pressure capillary rheometry, the sample is extruded through a cylindrical capillary die using a piston-driven setup. Due to instrumentation constraints of the round dies, the pressure transducer is typically located at the entrance of the capillary, and not along the die length. Consequently, the pressure reading at that point reflects

the total pressure drop required to drive the material through the capillary, leading to higher measured pressure gradient compared to pressure inside the capillary [35], which comprises two main components:

$$p = p_l + p_e \tag{3-1}$$

where:

- ullet p_l is the viscous pressure drop along the length of the capillary,
- $oldsymbol{p}_e$ is the entrance pressure loss, originating from the abrupt contraction from the piston diameter to the die diameter.

This entrance pressure drop p_e is not associated with viscous shear in the capillary but rather with a complex flow pattern including and secondary flows near the entrance region as shown in Figure 3.5. As such, it must be removed from the total pressure to determine the true shear-induced stress inside the capillary.

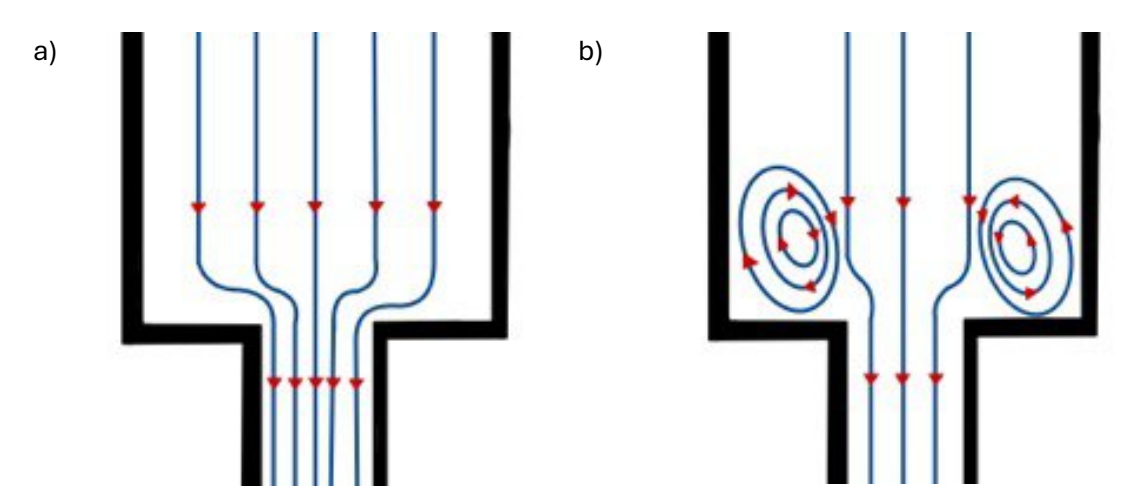


Figure 3.5) a) Newtonian Fluid b) Non-Newtonian Fluid

The Bagley correction, introduced by E.B. Bagley in 1957 [36], is an empirical method for estimating and subtracting the entrance pressure loss. The involves using capillaries of different lengths but identical diameters and performing rheological measurements under identical temperature and flow conditions. The total measured pressure is then plotted against the die length, and the resulting linear extrapolation to zero length yields the entrance pressure loss p_e :

$$p_{measured} = m.L + p_e (3-2)$$

Here:

- $p_{measured}$ is the pressure recorded by the transducer,
- L is the capillary length,
- m is the slope representing the pressure gradient along the capillary (Pa/mm),
- p_e is the y-intercept, indicating the entrance pressure loss (Pa).

The experimental procedure typically uses two or more capillaries in parallel measurements. In this work, two round dies were used: one with length L=20 mm, and another with short length L \approx 0.2 mm, effectively serving as a theoretical "zero-length" die. A theoretical zero-length capillary is characterized by a length-to-radius ratio of zero. Therefore, as the polymer melt passes through such a contraction, the flow immediately converges and diverges without traveling any meaningful distance. The channel is too short for the development of a fully established flow profile. In theory, the only pressure losses in a zero-length capillary arise from the entrance convergence and the exit divergence of the flow [37]. This design enables linear Bagley correction, assuming that the entrance pressure drop remains constant and independent of die length.

The data points from both dies are plotted as pressure versus length, and a linear regression is applied. The interception of this line at L = 0 directly gives the entrance pressure drop p_e . The corrected pressure drop due to viscous flow is then:

$$p = p_{measured} - p_e (3-3)$$

Once the entrance pressure loss is known, the true wall shear stress in the capillary can be computed using the corrected pressure drop:

$$\tau = \frac{p.\,R}{2.\,L} \tag{3-4}$$

where:

- τ the true wall shear stress (Pa),
- $p = p_{measured} p_e$ is the corrected pressure loss (Pa),

- R is the capillary radius (mm),
- L is the capillary length (mm).

This expression arises from the assumption of fully developed laminar flow in a cylindrical tube, where the shear stress at the wall is linearly proportional to the pressure gradient and the capillary radius.

In some cases, especially when three or more dies of varying lengths are used, a nonlinear Bagley correction may be applied to account for deviations from linear behavior. However, in this work, a linear Bagley correction was implemented, which is appropriate for most practical applications involving moderate aspect ratios and shear rates.

Figure 3.6 shows a representative Bagley plot, where pressure values obtained from the long and short dies at a specific temperature are plotted against their respective lengths. The linear extrapolation provides a clear estimate of p_e . As seen in Figure 3.7, application of Bagley correction results in a downward shift of the viscosity curve, indicating that the shear stress was previously overestimated due to uncorrected entrance losses.

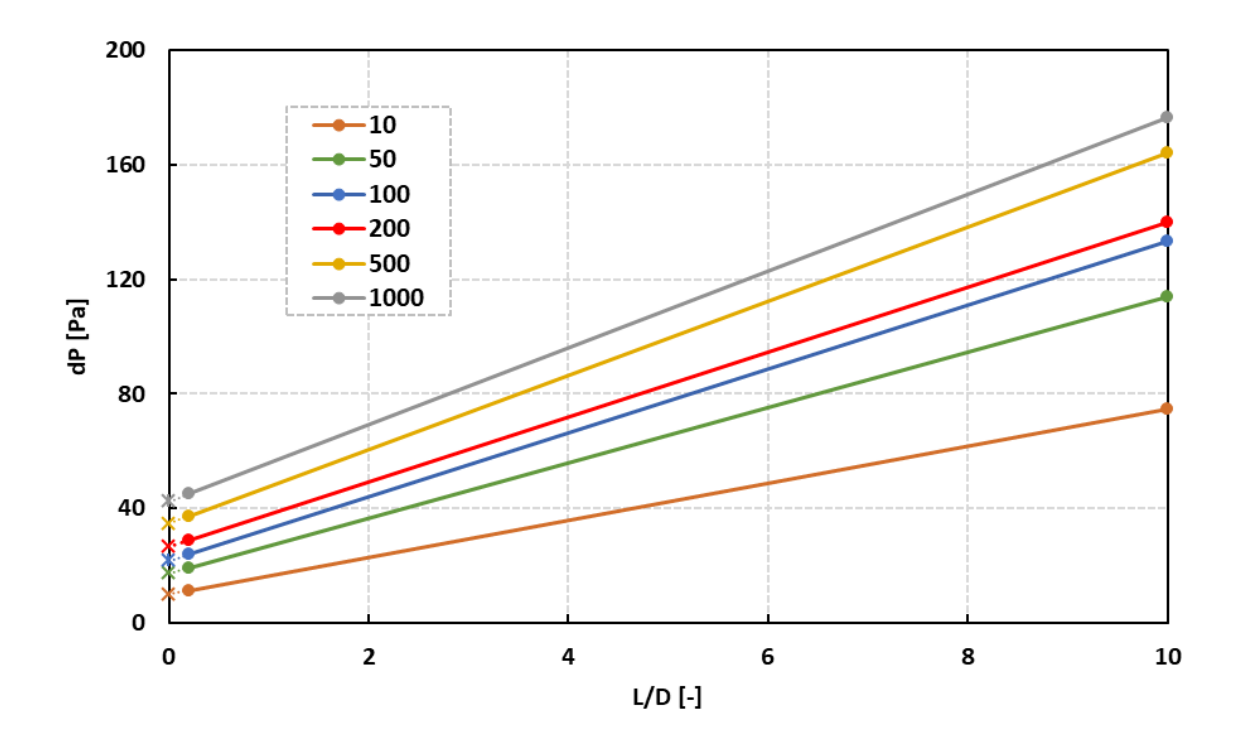


Figure 3.6) Linear Bagley correction plot

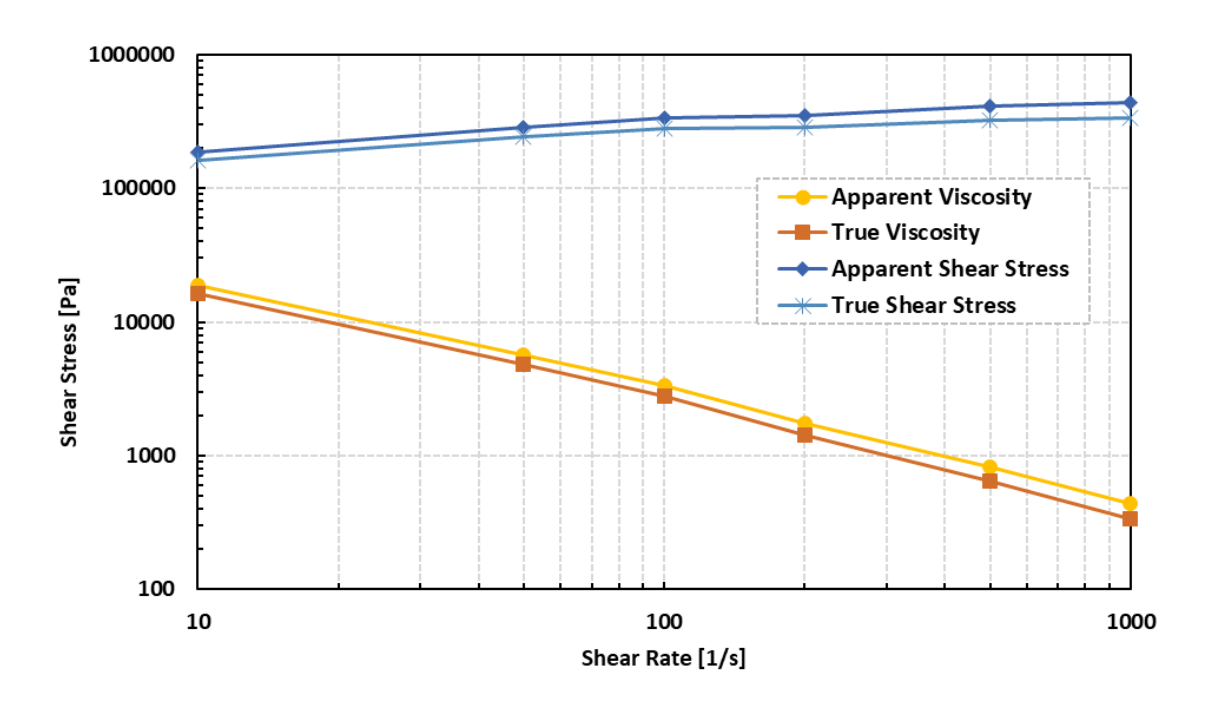


Figure 3.7) Shear stress corrected viscosity values

3.4 Weissenberg-Rabinowitsch Correction

To obtain true values of viscosity, the next step will be to determine true values of shear rate. While Bagley correction addresses the overestimation of wall shear stress due to entrance pressure losses, the apparent wall shear rate calculated under Newtonian assumptions remains a source of significant error for shear-thinning fluids. This discrepancy is addressed through the Weissenberg-Rabinowitsch correction, a mathematical formulation that adjusts the apparent shear rate to reflect the true velocity gradient at the capillary wall.

The default method in capillary rheometry estimates wall shear rate $\dot{\gamma}$ using the analytical expression for Newtonian fluids:

$$\dot{\gamma}_{app} = \frac{4.\,Q}{\pi.\,R^3} \tag{3-5}$$

where:

- Q is the volumetric flow rate (mm³/s),
- R is the capillary radius (mm).

This equation is derived from the parabolic velocity profile associated with fully developed laminar flow of Newtonian fluids in a cylindrical tube [38]. However, for non-Newtonian fluids, especially shear-thinning materials, the velocity profile becomes a function of viscosity, and the shear rate at the wall is underestimated if Newtonian assumptions are applied.

As a result, the viscosity $\eta(\dot{\gamma})=\frac{\tau}{\dot{\gamma}}$ calculated using apparent shear rate would be overestimated, compromising both model accuracy and subsequent simulations. The solution is to apply the Weissenberg-Rabinowitsch correction to obtain a more physically representative true wall shear rate.

The Weissenberg-Rabinowitsch (WR) equation is based on a generalized formulation for non-Newtonian laminar flow in a circular capillary. The true wall shear rate is given by [39]:

$$\dot{\gamma} = \frac{3n+1}{4n} \cdot \dot{\gamma}_{app} \tag{3-6}$$

Here, term **n** represents the logarithmic slope of the shear stress versus apparent shear rate curve and serves as a correction factor that adjusts for the deviation from Newtonian behavior. For a Newtonian fluid, this slope equals 1, and the correction reduces to the classical Newtonian case.

In practice, the WR correction is implemented numerically by fitting a log-log curve to the Bagley-corrected shear stress τ_w versus the apparent shear rate $\dot{\gamma}_{app}$. This step ensures that both pressure losses and non-Newtonian velocity profiles are accounted for in the final viscosity calculation.

In the current study, a 4th-order polynomial fit was applied to the $\log(\tau_w)$ vs $\log(\dot{\gamma}_{app})$ data. While a 2nd-order polynomial may be sufficient in many cases, the higher-order fit was chosen to enhance the smoothness of the gradient and avoid numerical instability [40].

Once the curve is fitted, the derivative of the fitted polynomial is computed numerically for each data point. This slope is then inserted into the WR equation to yield the corrected wall shear rate $\dot{\gamma}$.

Finally, the true shear viscosity is calculated as:

$$\eta(\dot{\gamma}) = \frac{\tau}{\dot{\gamma}} \tag{3-7}$$

The effect of WR correction is illustrated in Figure 3.8. As observed, the viscosity curves undergo a horizontal shift to the right, reflecting an increase in the computed shear rate due to the correction. This adjustment is particularly significant for high-viscosity fluids and at moderate to high shear rates, where the non-parabolic flow profile exerts a more pronounced effect.

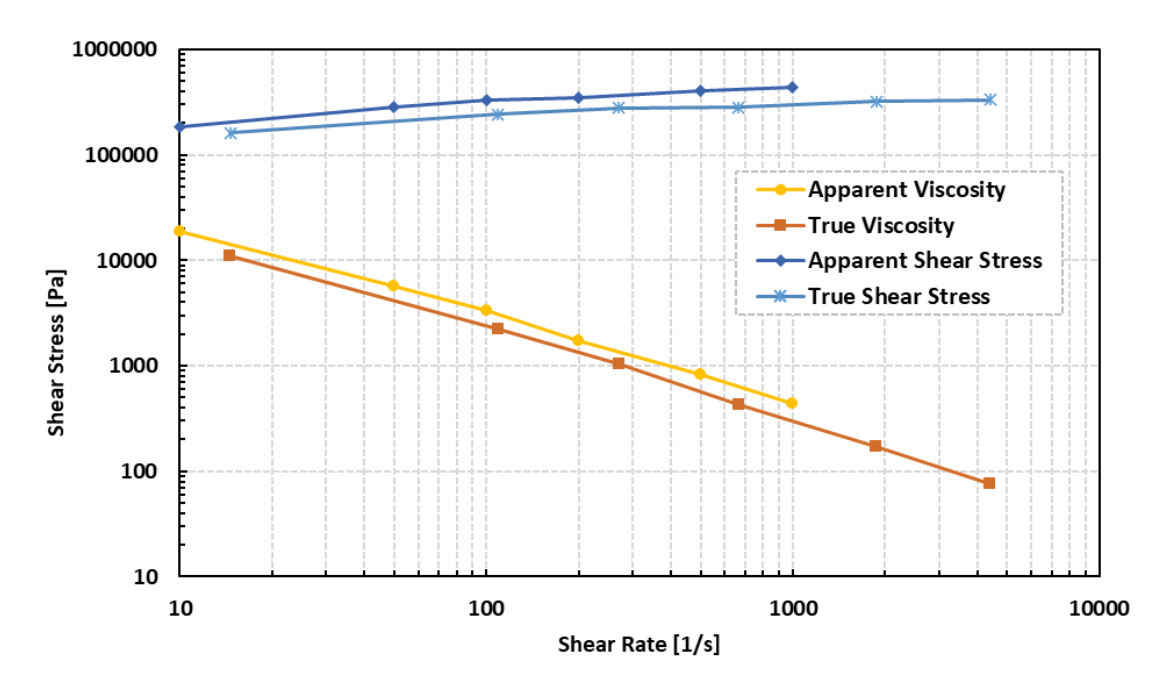


Figure 3.8) Shear rate corrected viscosity values

When combined with the Bagley correction (which shifts the curves downward by reducing wall shear stress), the WR correction ensures that both axes of the viscosity curve, stress and rate, are properly adjusted. The net result is a corrected viscosity curve that aligns closely with physical reality, thereby serving as a reliable basis for model development as can be seen in Figure 3.9.

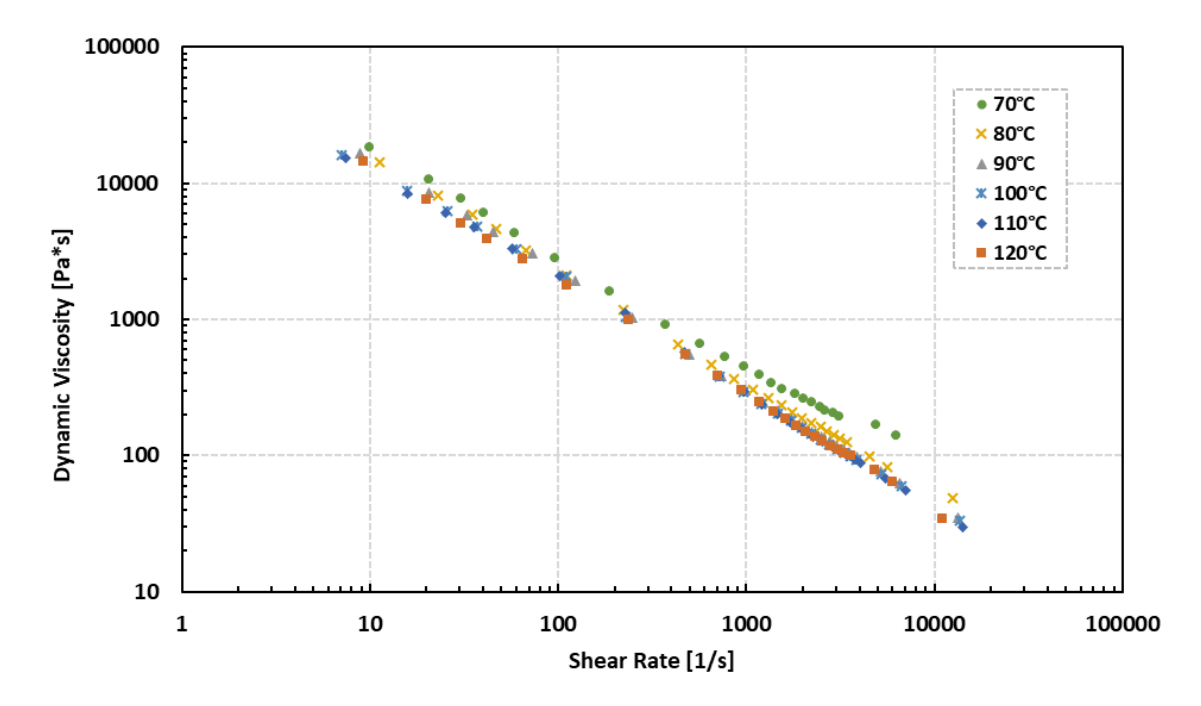


Figure 3.9) Corrected true viscosity data

The derivation and application of the Weissenberg-Rabinowitsch correction rest on several theoretical assumptions [40], [41]:

- The flow is steady, laminar, and fully developed within the capillary.
- The fluid is incompressible and obeys a generalized Newtonian model. Which means the viscosity is only the function of shear rate. Which indicates that the iso-thermal condition should be considered as an assumption.
- The flow is slippage free. In case of presence of slippage in the measured data points, the data should be slip-corrected before attempting to apply WR correction.

Additionally, the correction becomes more sensitive to data scatter and noise when implemented numerically, especially in the slope calculation. Therefore, the quality of curve fitting and the choice of polynomial order are critical in minimizing artifacts in the corrected shear rate.

Chapter 4 | Classical Viscosity Models for Shear-Thinning Fluids

This chapter provides a detailed overview of classical constitutive models used to describe the viscosity of shear-thinning fluids. Although both shear rate and temperature influence viscosity in real systems, traditional formulations typically treat these effects separately. Accordingly, the models presented here are categorized into two main groups: those that describe shear rate dependence and those that account for temperature dependence. The discussion highlights the theoretical foundations, assumptions, and applicability ranges of each formulation, providing the necessary background for the development of the unified model proposed later in this thesis. It should be noted that, due to instrumentation constraints in the experimental setup, the effects of pressure are not considered in this study [42].

4.1 Shear Rate-Dependent Viscosity Models

Shear-thinning fluids exhibit a non-linear decline in viscosity as the applied shear rate increases. This effect is physically attributed to molecular alignment, disentanglement, or breakdown of internal structures under flow. To capture this non-Newtonian behavior, several models have been developed, each with its own level of complexity, accuracy, and range of applicability.

4.1.1 Power Law Model

The Power Law model is one of the earliest and most intuitive models used to describe shear-thinning behavior. It is mathematically simple and involves only two fitting parameters: the consistency index K and the flow behavior index n. The Power Law model reads as:

$$\eta_{(\dot{\gamma})} = K \cdot \dot{\gamma}^{n-1} \tag{4-1}$$

The Power Law model is capable of describing both shear-thinning and shear-thickening behavior. The flow behavior index, n, tunes the model to describe both behaviors. By n < 1 the model fits on the shear-thinning fluid data and by n > 1 it describes shear-thickening materials. It's obvious that with n = 1 the dependency of the models in shear rate will cancel out and it eventually ends with a Newtonian constant viscosity. Therefore, the physical units of the flow consistency index K will be Pa.s and the flow behavior index is dimensionless. However, the dimensional inconsistency of the Power Law model is discussed in the paper published by PRENTICE, J. H. [43] which indicates another limitation of this model. This arises from the fact that K must absorb units of shear rate raised to a power, which varies with n.

Despite its computational efficiency and ease of implementation, the Power Law model has critical limitations. Notably, it does not predict the Newtonian plateau at low shear rates (zero-shear viscosity) and predicts infinite value for viscosity at shear rate equal to zero. Likewise, it fails to represent a second plateau at high shear rates, a region that some complex fluids do exhibit. These shortcomings limit their usefulness in full-range rheological characterizations, especially in CFD applications where numerical instability can result from infinite or undefined viscosities at shear rate boundaries.

4.1.2 Carreau Model

To address the deficiencies of the Power Law model, the Carreau model [44] introduces a more flexible three-parameter form. It smoothly transitions between Newtonian behavior at low shear rates and Power Law behavior at higher shear rates. The functional form is expressed as:

$$\eta_{(\dot{\gamma})} = \eta_0 \cdot (1 + (\lambda \dot{\gamma})^2)^{\frac{(n-1)}{2}}$$
(4-2)

where:

- η_0 is the zero-shear viscosity (Pa·s),
- λ is the relaxation time (s), indicating the inverse of the critical shear rate, at which the shear-thinning behavior is triggered.
- n is the flow behavior index (dimensionless).

This model provides a more complete description of the flow curve and is well-suited to many polymeric systems, as it inherently captures the Newtonian plateau at low shear and the shear-thinning region without asymptotic divergence. At very high shear rates, however, the model may still predict a continuous decrease in viscosity, which does not correspond to the finite viscosity plateau observed in some materials. In order to enable the model to predict the second Newtonian plateau at high shear rates, the Carreau-Yasuda model was introduced [45].

4.1.3 Cross Model

The Cross model offers an alternative to Carreau with a slightly simplified structure. Unlike Carreau model that assumes quadratic dependency on the shear rate through $(\lambda\dot{\gamma})^2$ term, the Cross model assumes a simpler linear relationship between viscosity and shear rate through $(\lambda\dot{\gamma})$ [46] or $\left(\frac{\eta_0}{\tau^*}\dot{\gamma}\right)$ [47]and can be written as [47]:

$$\eta_{(\dot{\gamma})} = \frac{\eta_0}{1 + \left(\frac{\eta_0 \cdot \dot{\gamma}}{\tau^*}\right)^{1-n}} \tag{4-3}$$

The Cross model is claimed to be a simplified form of Carreau model, also known as Bird-Carreau [46]. where η_0 remains the zero-shear viscosity, n is the Power Law index, and τ^* is the characteristic shear stress, and it mostly depends on chemical properties

of the material [48] and identifies a shear stress at which the transition to non-Newtonian behavior begins.

The Cross model is widely employed in polymer processing simulations and rheological measurements. Compared to the Carreau model, it provides a different curvature for the transition region. It is particularly effective for modeling fluids in industrial extrusion, molding, and mixing applications.

4.2 Temperature-Dependent Viscosity Models

Temperature plays a fundamental role in determining the viscosity. For polymeric systems, temperature influences both molecular mobility and chain entanglement, resulting in a highly non-linear response of viscosity. It is worth mentioning that the effect of temperature on viscosity is also considered in the case of a Newtonian flow. In liquids, an increase in temperature will result in a decrease in viscosity. However, in gaseous fluids the viscosity increases with an increase in temperature. The reason for this behavior is that the definition of viscosity in gases is considered as random collision of gas molecules which creates a resistance to flow, and these random motions increase by increasing temperature. The effect of temperature on the viscosity of a non-Newtonian fluid makes this property highly-nonlinear and complex. In this section, some of the mostly used temperature dependency models will be discussed in detail.

4.2.1 Arrhenius Model

The Arrhenius model is one of the most straightforward representations of temperature-dependent viscosity, assuming an exponential decay in viscosity with increasing temperature. Its classical form is [49]:

$$\eta_{(T)} = \eta_a \cdot e^{\left(\frac{E_a}{R \cdot T}\right)} \tag{4-4}$$

where:

• η_a is the pre-exponential factor or viscosity in a reference temperature (Pa·s),

- E_a is the activation energy for viscous flow (J/mol),
- R is the universal gas constant (8.314 J/mol·K),
- T is the absolute temperature in Kelvin.

The model is particularly valid for simple liquids or low-molecular-weight polymer melts. However, in most non-Newtonian fluids, the model fails to accurately predict the viscosity in temperatures near glass transition temperature T_g . This behavior is mainly due to the temperature-dependent nature of the activation energy [50].

4.2.2 Vogel-Fulcher-Tammann (VFT) Equation

Vogel–Fulcher–Tammann (VFT) is basically another representation of Arrhenius-type equation which incorporates a reference temperature. It means that the model can have better accuracy if we input measured viscosity in a specific temperature and then fit the model to the experimental data. The VFT equation can be written as [51]:

$$\eta_{(T)} = \eta_0 \cdot e^{\left(\frac{E_0}{R \cdot (T - T_0)}\right)} \tag{4-5}$$

The equivalence between the Arrhenius and VFT equations can be demonstrated through mathematical manipulation when the reference temperature is embedded in the exponential term, aligning their predictive behavior under certain conditions.

4.2.3 Williams-Landel-Ferry (WLF) Equation

For polymeric fluids in the temperature range close to T_g [52], the WLF model is more appropriate. Unlike the Arrhenius model, WLF is derived from the time–temperature superposition principle and is particularly applicable to amorphous polymers [53]. The model is given as:

$$\eta_{(T)} = \eta_0 \cdot e^{\left(-\frac{C_1 \cdot (T - T_g)}{C_2 + (T - T_g)}\right)}$$
(4-6)

where:

- C1 and C2 are model variables and should be determined via curve fitting,
- T_q is the glass transition temperature.

This equation is especially useful when modeling materials over a narrow range near T_g , and it implicitly reflects the molecular free volume theory. As polymers undergo relaxation near T_g , the viscosity change becomes highly nonlinear and the WLF model excels in this transitional domain.

The WLF model is capable of capturing the effects of both temperature and pressure. In applications where pressure also affects viscosity (as it alters T_g), a pressure-dependent version of the WLF equation can be used [47]:

$$T_a = D_2 + D_3.P (4-7)$$

where D_2 denotes the value of glass transition temperature at atmospheric pressure and D_3 is related to polymer's compressibility. However, for many practical applications, especially in atmospheric conditions, pressure dependence is neglected, therefore the equation is reduced to the standard WLF equation as:

$$T_q = D_2 (4-8)$$

4.3 Combined Shear Rate and Temperature-Dependent Models

Since viscosity in realistic polymer processing is simultaneously influenced by shear rate and temperature, it is often necessary to combine the aforementioned models to achieve predictive capability over the entire process domain. It can be claimed that zero shear viscosity η_0 , follows an Arrhenius-Type behavior [54] and WLF model is also capable of describing such behavior [55]. This approach results in multi-variable constitutive models, which blend shear-rate sensitivity (e.g., Carreau or Cross) with temperature-dependence (e.g., Arrhenius or WLF). The final formulation of Multi-Variable Constitutive models can be seen in Table 4-1.

Table 4-1) Multi-Variable constitutive viscosity models

Arrhenius

WLF

Carreau	$\eta_0 \cdot e^{\frac{E}{R \cdot T}} \cdot (1 + (\lambda \cdot \dot{\gamma})^2)^{\frac{n-1}{2}}$	$\eta_0 \cdot e^{\left(-\frac{c_1 \cdot (T - T_g)}{c_2 + (T - T_g)}\right)} \cdot (1 + (\lambda \cdot \dot{\gamma})^2)^{\frac{n-1}{2}}$
Cross	$\frac{\eta_0 \cdot e^{\frac{E}{R \cdot T}}}{1 + \left(\frac{\eta_0 \cdot e^{\frac{E}{R \cdot T}} \cdot \dot{\gamma}}{\tau^*}\right)^{1 - n}}$	$\frac{\eta_0 \cdot e^{\left(-\frac{c_1 \cdot (T - T_g)}{c_2 + (T - T_g)}\right)}}{1 + \left(\frac{\eta_0 \cdot e^{\left(-\frac{c_1 \cdot (T - T_g)}{c_2 + (T - T_g)}\right)} \cdot \dot{\gamma}}{\tau^*}\right)^{1 - n}}$
Power Law	η_0 . $e^{rac{E}{R \cdot T}}$. $\dot{\gamma}^{n-1}$	η_0 . $e^{\left(-\frac{c_1\cdot(T-T_g)}{c_2+(T-T_g)}\right)}.\dot{\gamma}^{n-1}$

This formulation retains the shear-thinning flexibility of the shear rate dependency models while accurately capturing thermal effects.

Despite their descriptive power, these composite models involve complex formulations and nonlinear terms, especially exponential functions, that are computationally intensive for numerical solvers. As discussed in the present study, this computational burden has motivated the development of a simplified model which aims to retain accuracy while improving efficiency.

Chapter 5 | Curve Fitting Methodology

Accurate determination of model parameters is essential for translating theoretical viscosity formulations into predictive tools. In this thesis, curve fitting is employed to calibrate classical viscosity models using the corrected rheological measurements obtained from high-pressure capillary experiments. Among the available optimization methods, nonlinear least squares (NLLS) fitting remains the most widely applied and theoretically grounded approach for parameter estimation in nonlinear systems [56].

This chapter presents the mathematical formulation of the NLLS problem, discusses numerical strategies for its solution, and explains the implementation using the lmfit package in Python. Particular emphasis is placed on parameter initialization, constraint handling, and convergence diagnostics, which are critical for ensuring both numerical stability and physically meaningful results.

5.1 Theoretical Basis of Nonlinear Least Squares

The nonlinear least squares problem is a generalization of linear regression where the dependent variable y is modeled as a nonlinear function of one or more independent variables x, and a set of parameters β . The objective is to find the parameter vector $\beta \in \mathbb{R}^p$ that minimizes the sum of the squared differences between the observed data and the model predictions.

Mathematically, the problem is posed as:

$$\min_{\beta} RSS(\beta) = \sum_{i=1}^{n} [y_i - f(x_i; \beta)]^2$$
 (5-1)

Where:

- $f(x_i; \beta)$ is the nonlinear model function (e.g., Carreau or Arrhenius)
- ullet y_i is the measured viscosity at the i-th shear rate and temperature
- x_i contains the independent variables $(\dot{\gamma},T)$
- n is the number of data points
- RSS denotes the Residual Sum of Squares

The goal is to find the set of parameters β that minimizes this residual sum. Unlike linear regression, however, no closed-form analytical solution exists for the minimizer of RSS in the general nonlinear case.

5.2 Iterative Numerical Solution

To solve the nonlinear least squares problem, iterative numerical algorithms are employed. The two most commonly used methods are the **Gauss-Newton algorithm** and the **Levenberg-Marquardt algorithm**, both of which approximate the nonlinear model using local linearization.

Let us denote:

•
$$r(\beta) = \begin{bmatrix} y_1 - f(x_1; \beta) \\ y_2 - f(x_2; \beta) \\ \vdots \\ y_n - f(x_n; \beta) \end{bmatrix}$$
 as the residual vector,

• $J\in R^{n imes p}$ as the Jacobian matrix of partial derivatives with elements $J_{ij}=rac{\partial f(x_i;eta)}{\partial eta_i}$

In the Gauss-Newton method, the update rule is:

$$\beta^{(k+1)} = \beta^{(k)} + \delta^{(k)}$$
 where $\delta^{(k)} = (J^{\mathsf{T}}J)^{-1}J^{\mathsf{T}}r$ (5-2)

This method assumes the model behaves nearly linearly near the solution. For highly nonlinear problems or when convergence stalls, the **Levenberg-Marquardt algorithm** introduces a damping term to stabilize the inversion:

$$(I^{\mathsf{T}}I + \lambda I)\delta = I^{\mathsf{T}}\mathbf{r} \tag{5-3}$$

Here, λ is an adaptive parameter that transitions between $\lambda \rightarrow 0$ (Gauss-Newton) and $\lambda \rightarrow \infty$ (Gradient Descent).

These updates are repeated iteratively until convergence, typically assessed by:

- Reduction in RSS below a threshold
- Change in parameter vector below a threshold
- Maximum number of iterations

5.3 Practical Considerations in Viscosity Model Fitting

When fitting rheological models like Carreau, Cross, or Arrhenius to experimental data, several practical challenges arise:

- 1. **Parameter Sensitivity**: Viscosity models contain parameters with strong nonlinear effects (e.g. λ , n, η_0), which can lead to ill-conditioned optimization landscapes.
- 2. **Physical Bounds**: Some parameters must stay within physically meaningful ranges (e.g., λ cannot be negative as the units are second).
- 3. **Initial Guess Sensitivity**: Convergence and accuracy depend significantly on the choice of initial parameter estimates.
- 4. **Heteroscedastic Errors**: Viscosity measurements often have higher uncertainty at low shear rates, violating assumptions of constant variance. This

behavior may bias the fitting process toward high-shear data unless weighting or error modeling is considered.

To manage these challenges effectively, we employ the lmfit library in Python, which is specifically designed for flexible and robust nonlinear curve fitting.

5.4 Imfit Python Library

The lmfit package is a high-level wrapper around SciPy's optimization routines, especially scipy.optimize.least_squares, offering several key benefits tailored to scientific modeling [57]:

- Named Parameters: Parameters can be labeled, constrained, and bounded explicitly.
- Bounds and Constraints: Physically meaningful limits (e.g., $\lambda>0$) can be applied easily.
- **Initial Value Handling**: It allows precise control over starting values, which is crucial for convergence.
- **Composite Models**: Multiple model components (e.g., Carreau + Arrhenius) can be defined symbolically and linked.
- Fit Statistics: Returns comprehensive metrics including:
 - R-squared
 - Reduced chi-squared
 - AIC and BIC
 - Confidence intervals via covariance estimation

5.5 Fit Results and Model Selection

Following the implementation of the nonlinear least squares curve fitting procedure using the lmfit Python library, a set of classical viscosity models were evaluated for their ability to accurately capture the rheological behavior of the elastomeric compound. Among these, the Carreau–Arrhenius model was selected as the most

appropriate baseline due to both its physical consistency and its superior numerical performance across the shear rate and temperature range.

The mathematical form of the Carreau–Arrhenius model used in this study is as follows:

$$\eta(\dot{\gamma}, T) = \eta_0 \cdot e^{\frac{E}{R \cdot T}} \cdot (1 + (\lambda \cdot \dot{\gamma})^2)^{\frac{n-1}{2}}$$
 (5-4)

Where:

η: dynamic viscosity [Pa·s]

 $\dot{\gamma}$: shear rate [s^{-1}]

T: absolute temperature [K]

 η_0 : zero-shear viscosity [Pa·s]

E: activation energy [J/mol]

R: universal gas constant [8.314 J/mol·K]

 λ : characteristic time constant [s]

n: flow behavior index [-]

To ensure physically meaningful and numerically stable results, parameter bounds were imposed during the fitting process:

$$0 < \eta_0$$
, $0 < E$, $0 < \lambda$, $0 < n < 1$

In particular, the upper bound on the flow behavior index n was chosen to reflect the shear-thinning nature of the compound, ensuring that the model did not converge to Newtonian or shear-thickening behavior. Initial guesses for all parameters were chosen based on ranges reported in the literature for similar elastomeric systems. This was necessary to reduce computational cost and minimize the risk of divergence in the optimization routine, especially given the non-convex nature of the residual surface.

After optimization, residual plots were inspected to confirm the absence of systematic trends, and confidence intervals were extracted from the covariance matrix of the fit to assess the statistical significance of the model parameters. The final fitted curve

displayed excellent agreement with the experimental viscosity data across the tested shear rates and temperatures. This performance is illustrated in Figure 5.1, which shows the model fit over the original experimental dataset, confirming its ability to capture the measured rheological behavior with high fidelity.

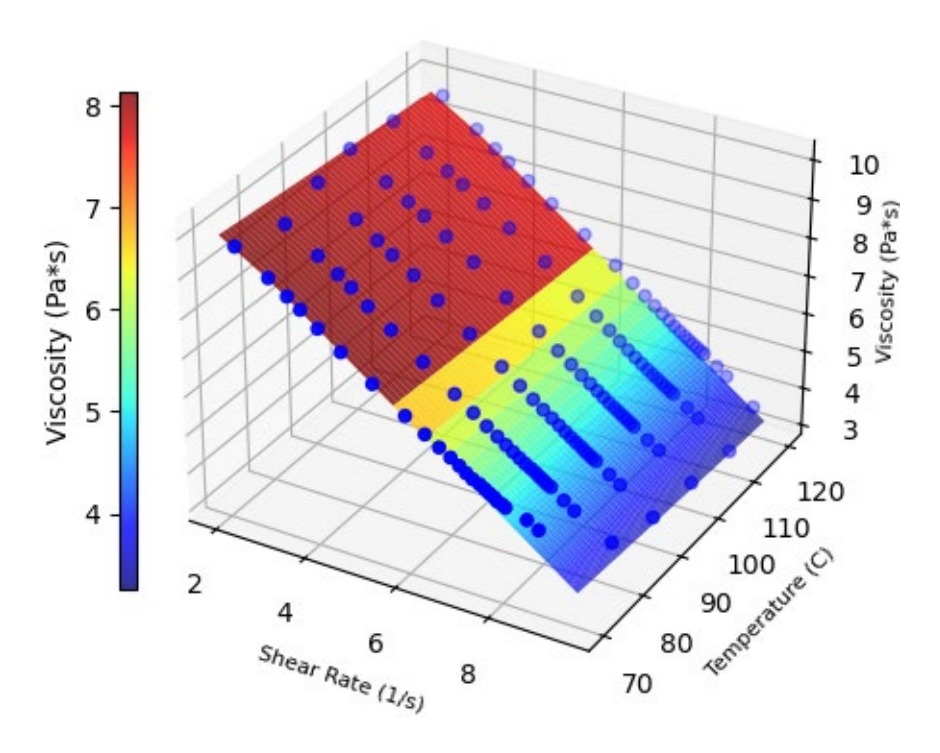


Figure 5.1) Carreau-Arrhenius model fit results on corrected viscosity data. Shear

Rate and Viscosity are in Logarithmic scale.

To further assess the physical validity and extrapolation capability of the model, an additional evaluation was performed beyond the experimental range. Specifically, the Carreau–Arrhenius model was extrapolated over a broader shear rate domain, extending into the low-shear region where the Newtonian plateau is expected. The result, shown in Figure 5.2, demonstrates that the model correctly predicts asymptotic behavior at low shear rates, reinforcing its suitability as a benchmark for comparison with the proposed MVI model.

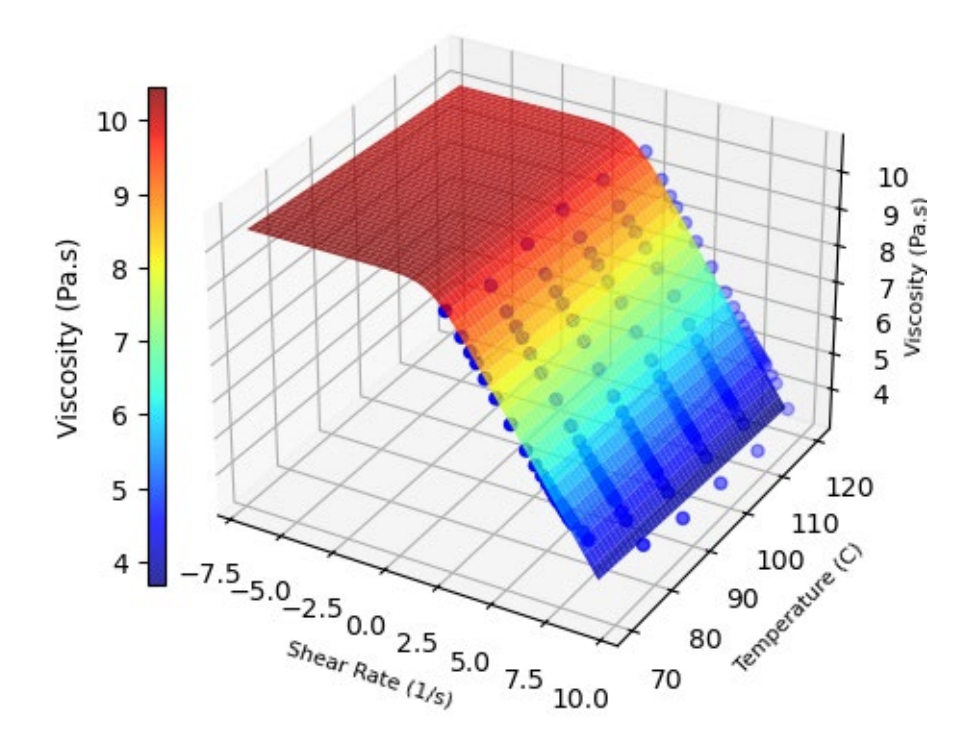


Figure 5.2) Extrapolation of Carreau-Arrhenius model fit results on corrected viscosity data. Shear Rate and Viscosity are in Logarithmic scale.

Figure 5.3 and Figure 5.4 show the viscosity contour of Carreau-Arrhenius model to our corrected viscosity data. Temperature dependency behavior on all three rheological regions including Newtonian plateau, transition region and shear-thinning regime can be observed.

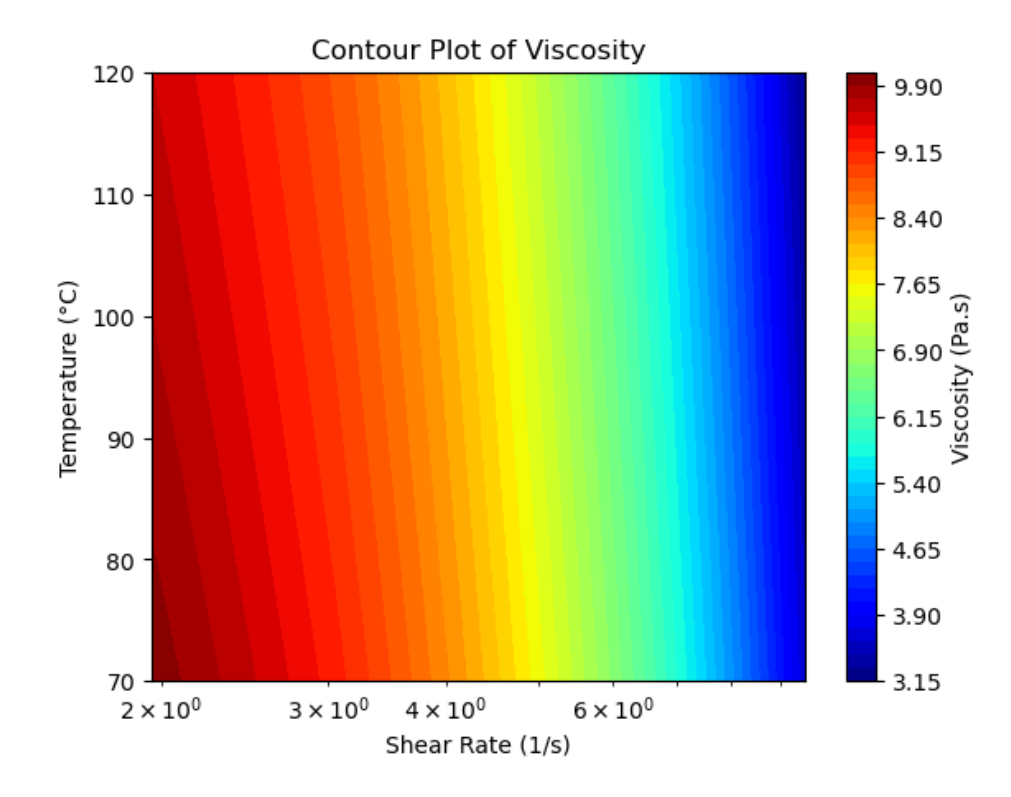


Figure 5.3) Carreau-Arrhenius model viscosity contour on final corrected viscosity

data

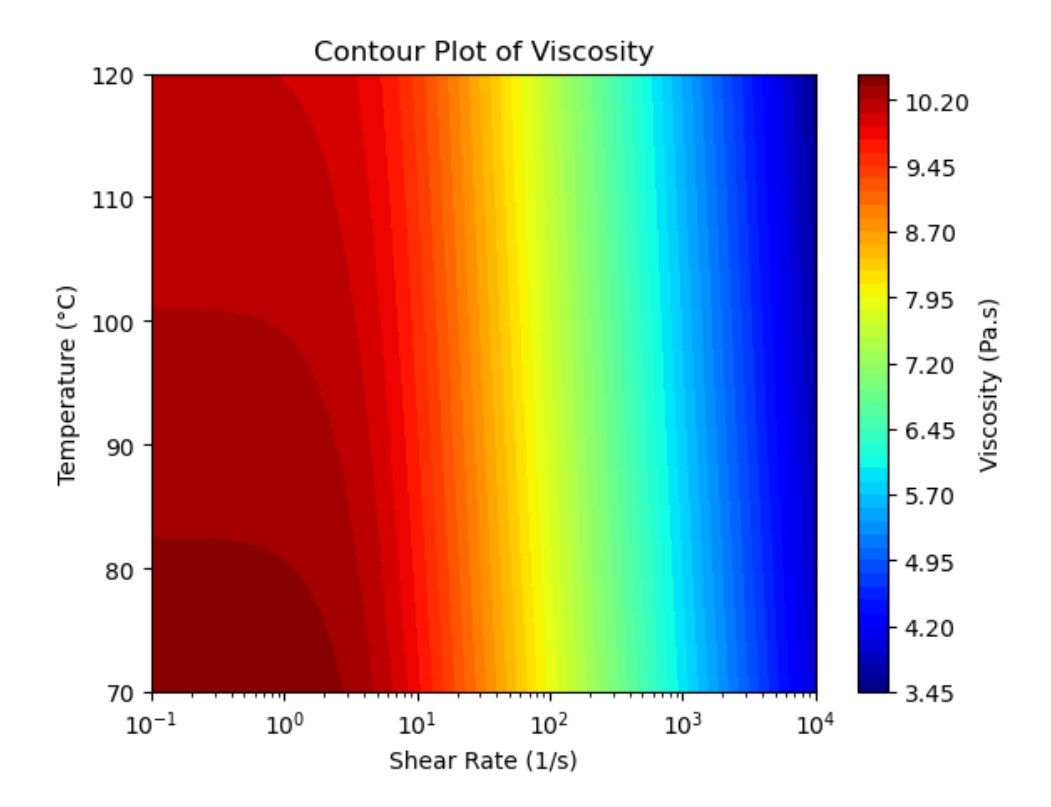


Figure 5.4) Extrapolation of Carreau-Arrhenius model viscosity contour on final corrected viscosity data

Fit statistics at Table 5-1 show final obtained model variables from the corrected dataset. The extracted fit parameters from the extrapolated fit served as the source of synthetic data generation for training the MVI model, as discussed in the following chapter.

Table 5-1) Extracted fit parameters of Carreau-Arrhenius model from the corrected dataset

Carreau-Arrhenius

n[-] 0.14 E[J/mol] 8968 $\eta_0[Pa. s]$ 1505 $\lambda[s]$ 0.195

Several classical models were initially considered during the model selection process. While the Power Law model provides a basic approximation for shear-thinning fluids, it fails to represent the Newtonian plateau observed at low shear rates. This limitation is particularly important in the present context, as both the experimental data and the final MVI model exhibit a continuous transition between Newtonian and non-Newtonian behavior. Therefore, the Power Law model was excluded from further analysis.

The Cross and Carreau models are both capable of capturing the full viscosity curve, differing mainly in the curvature of the transition region. In this study, the Carreau model demonstrated a better fit across the full range of shear rates and hence was selected as the shear-rate dependency component. The Arrhenius temperature dependency was preferred over the WLF model due to the low glass transition temperature (approximately –50 °C) of the compound. Since all measurements were taken well above T_g , the Arrhenius formulation is more appropriate and avoids unnecessary parameter inflation associated with the WLF equation, which is typically suited for behavior close to T_g .

The **Carreau–Arrhenius** model was selected as the classical benchmark for subsequent comparisons, including the symbolic regression-based MVI model developed in later chapters. The model not only provided a high-fidelity fit to the experimental data but also maintained a compact parameter set and physical interpretability.

Chapter 6 | Data Preparation and Train-Test Partitioning

The development of any data-driven model critically depends on the quality, diversity, and physical consistency of the dataset on which it is trained. In this work, data preparation forms the foundation of model discovery, ensuring that the resulting viscosity model is both generalizable and physically meaningful. To achieve comprehensive coverage of the relevant rheological regimes, including the Newtonian plateau, transition region, and pseudoplastic domain, a combined dataset was constructed using experimental measurements and synthetic data generated from a validated classical formulation.

This chapter describes the procedures used to assemble, preprocess, and normalize the data prior to model training. It also outlines the strategy adopted for dividing the dataset into training and test subsets, ensuring that both domains adequately represent the range of shear-rate and temperature conditions required for model development in the following chapter. The experimental limitations of the high-pressure capillary rheometer, particularly its restricted low-shear resolution, are discussed, along with the complementary strategy employed to overcome them through the generation of synthetic data from a validated classical model.

6.1 Limitations of Experimental Data

Despite the high quality of the capillary rheometry data, a key limitation became evident: the measurements were concentrated in the shear-thinning region. Due to the material's very low zero-shear viscosity and the physical limitations of the capillary method, it was not possible to obtain experimental data in the low-shear Newtonian plateau or the intermediate transition zone.

This posed a serious challenge for downstream symbolic regression. When training data lacks these key regions, symbolic models are prone to overfitting to monotonic or power-law–like behavior, making them incapable of capturing zero-shear viscosity or smooth curvature. Furthermore, models without plateau behavior exhibit singularities or unstable behavior at low shear rates, compromising their usability in CFD solvers.

6.2 Synthetic Dataset Generation

The **Carreau–Arrhenius** model was chosen not only for its good fit to the data but also for its physical plausibility and compatibility with the expected viscosity behavior across shear and temperature domains.

Using the best-fit parameters, a synthetic dataset of ~2000 points was generated. This dataset was:

- Logarithmically spaced in shear rate (to emphasize both plateau and highshear regions)
- Spread across the temperature range of experimental data
- Explicitly included a data point at $\dot{\gamma}=0$ to define zero-shear viscosity
- Temperature was incremented by 2 °C to allow the model to better learn temperature behavior.

This ensures that the symbolic regression algorithm is not only trained across all relevant physical regimes, but is also penalized if it attempts to generate singularities near zero shear.

6.3 Final Dataset Composition and Balancing

The final dataset used to train the MVI model was composed of two parts:

- **Synthetic data:** Derived from the validated Carreau–Arrhenius model, covering the entire shear-viscosity curve uniformly
- Experimental data: Measured values corrected for entrance and shear-rate artifacts

To prevent model bias toward either dataset, a weighted loss function was implemented in the symbolic regression routine. This ensures that the discovered expression reflects both:

- The empirical accuracy of real-world measurements
- The structural realism and smoothness offered by the synthetic data

This composite dataset provides an ideal balance between experimental fidelity and full-domain coverage, enabling the symbolic regression algorithm to discover a model that is both physically interpretable and numerically robust.

6.4 Train-Test Split Strategy

A robust and physically consistent symbolic model must not only fit the training data but also generalize to unseen data points. To this end, the dataset was divided into two subsets: a training set and a test set. Approximately 70% of the total data was used for training, serving as the foundation for model discovery. The remaining 30% was withheld from the training process and later used to evaluate the generalization capability of the final discovered model.

This split ratio (70/30) is consistent with findings in machine learning theory, particularly in symbolic regression literature, where the accuracy of tree-based search methods depends more on the diversity and coverage of the training set than on sheer volume [58]. Furthermore, the test set provides a good measure of generalizability of the model, being able to be fit on the unseen data without being overfit to the training set.

6.5 Final Preprocessing Steps

Before feeding the dataset into the symbolic regression engine (PySR), several final transformations were applied:

Log-transformation of shear rate and viscosity:

$$x = \log_{10}(\dot{\gamma}), y = \log_{10}(\eta)$$

This reduces dynamic range and linearizes power-law-like behavior, improving convergence and reducing overfitting.

• Standardization:

- o Input variables ($\dot{\gamma}$, T) were standardized to zero mean and unit variance
- This helps in maintaining numerical stability during symbolic regression and ensures gradient-based operations remain well-scaled

This precise approach to data preparation ensured that the symbolic regression algorithm would discover an interpretable, generalizable, and physically meaningful viscosity model, setting the stage for the derivation of the MVI equation in the next chapter. Figure 6.1 shows the final data set for the model training, before 70/30 splitting.

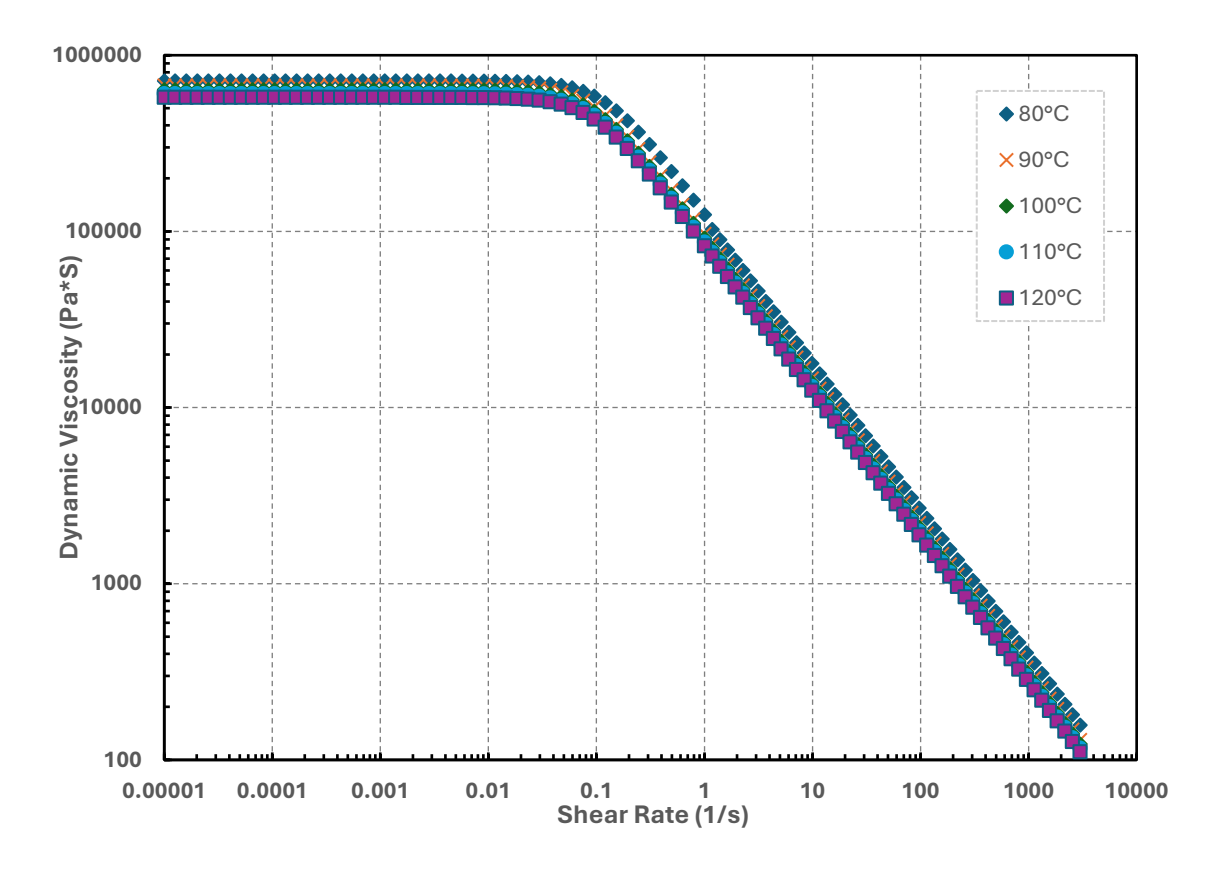


Figure 6.1) A sample of final synthetic data set

Chapter 7 | **Symbolic Regression**

This chapter introduces symbolic regression as the central data-driven methodology for discovering explicit viscosity models. The chapter begins with a conceptual overview of symbolic regression and a review of the principal algorithms historically used for equation discovery, including genetic programming, simulated annealing, Bayesian methods, and heuristic search approaches. It then formalizes the learning problem and defines the evaluation metrics adopted in this study. Finally, the implementation of symbolic regression through the PySR framework is presented, followed by the derivation and assessment of the Multi-Variable Implicit (MVI) model proposed in this thesis.

7.1 Introduction to Symbolic Regression

Symbolic Regression (SR) represents a class of machine learning techniques that seek not only to fit data but to uncover the underlying mathematical structure governing a system. Unlike traditional regression methods that assume a predefined form for the function (e.g., linear, polynomial, or exponential), symbolic regression attempts to discover both the optimal structure and parameters of the model simultaneously. This task is particularly appealing in scientific disciplines where interpretability, physical insight, and mathematical simplicity are as important as predictive accuracy. Symbolic regression belongs to the class of evolutionary algorithms and differs from traditional regression methods by directly generating analytical formulas from data without requiring prior assumptions about model structure [59]. This approach not only enhances flexibility but also delivers physically meaningful models that are ideal for integration into numerical solvers. The symbolic expressions it produces can maintain smoothness, differentiability, and compactness.

The symbolic regression problem is formally defined as follows: given a set of inputoutput pairs $(X, y) = \{(x_i, y_i)\}_{i=1}^n$, with $x_i \in R^d$, $y_i \in R$, and assuming the outputs are generated by an unknown function $y_i = f(x_i) + \epsilon_i$, the goal is to discover an expression $g(\cdot)$ such that $g \approx f$ over the domain of interest. The challenge lies in the fact that the function space \mathcal{F} is effectively infinite and contains arbitrarily complex expressions composed of arithmetic, algebraic, and transcendental functions.

Two key objectives guide symbolic regression:

- 1. **Accuracy**: The expression should minimize the discrepancy between predicted and actual outputs, typically measured via metrics such as RMSE, MAE, or R^2 .
- 2. **Simplicity**: The expression should be as concise and interpretable as possible, aligning with the principle of Occam's razor.

These objectives are often in tension; increasing complexity generally improves fitness but reduces interpretability. To balance this trade-off, Pareto optimization is used. It identifies the set of best possible compromises, called the Pareto front, where no solution can be both more accurate and simpler at the same time.

7.2 Classical Methods in Symbolic Regression

7.2.1 Genetic Programming

Symbolic regression as a formalized computational method emerged prominently with the work of John Koza [60] in the early 1990s through the paradigm of Genetic Programming (GP). GP treats candidate mathematical expressions as "individuals" in a population, each represented by a tree structure. Internal nodes of the tree correspond to operators (e.g., +, -, ×, sin, exp), while leaves correspond to variables or constants.

GP constructs candidate models as expression trees, where primitive functions (e.g., +, ×, log) are internal nodes and variables/constants are terminal nodes. This structure allows symbolic regression to evolve new equations by applying biologically inspired operations such as mutation and crossover [61]. A visual representation of this structure is shown in Figure 7.1, which illustrates how symbolic expressions are constructed as rooted trees. The internal nodes represent mathematical operators, while the leaves contain constants and variables.

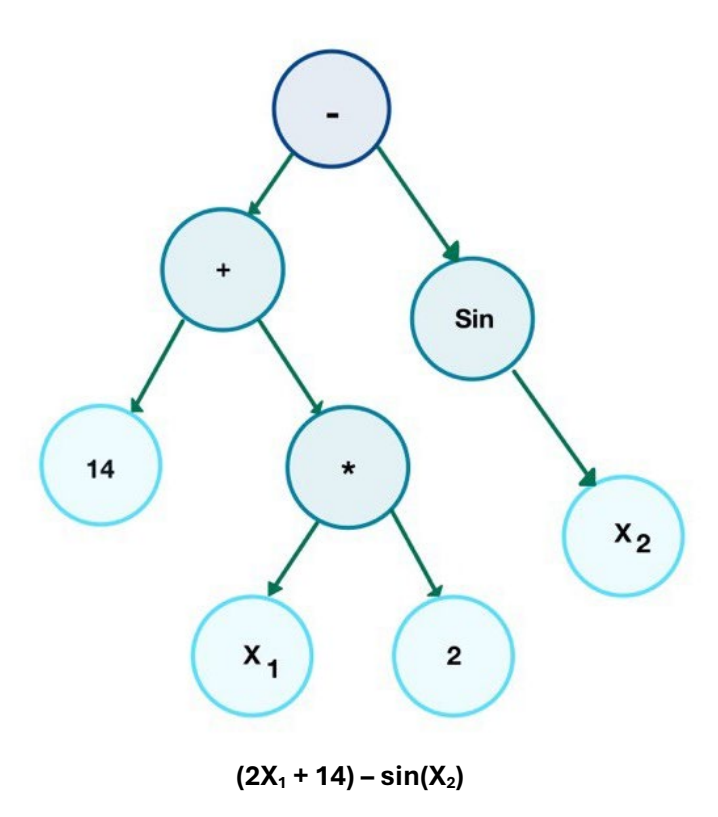


Figure 7.1) Tree-Shaped symbolic regression algorithm structure.

The GP algorithm iteratively evolves the population via biologically inspired operators:

- **Crossover**: Randomly exchanges subtrees between parent expressions.
- **Mutation**: Replaces a randomly selected subtree with a new, randomly generated one.
- **Selection**: Chooses individuals based on a fitness function (e.g., low RMSE and low complexity).

This approach enables the exploration of vast search spaces without requiring prior assumptions on the model structure. However, it suffers from several drawbacks:

- **Premature convergence**: Populations can converge to suboptimal solutions early in the evolution.
- **Computational cost**: Evaluating and mutating large expression trees is resource-intensive.
- Overfitting: Complex trees may fit noise in the data.

Nonetheless, GP remains a foundational approach. Tools such as GPTIPS [62], Al Feynman [63], Eureqa [64], Operon [65], and gplearn [66] have improved upon the basic GP paradigm by incorporating linear scaling, semantic backpropagation, neural-symbolic hybridization, multi-tree ensembles, and C++ optimization for faster execution.

7.2.2 Simulated Annealing

Simulated Annealing (SA) offers another metaheuristic strategy for SR. Inspired by the physical annealing process in metallurgy, SA explores the solution space by stochastically accepting worse solutions based on a "temperature" parameter that gradually cools. The idea is to avoid local minima early in the search and gradually refine solutions as the temperature drops.

SA-based symbolic regression typically perturbs expressions via defined neighborhood function such as modifying an operator or constant, and accepts changes based on a Metropolis criterion. While less common than GP, SA can yield

competitive results, especially when combined with handcrafted priors or domainspecific knowledge, as seen in software like TuringBot.

7.2.3 Bayesian Methods

Bayesian symbolic regression attempts to infer posterior distributions over expression trees given observed data. This involves defining a prior over expressions typically via a context-free grammar, and using Markov Chain Monte Carlo (MCMC) or Metropolis-Hastings algorithms to sample from the posterior.

This approach naturally incorporates uncertainty and prior knowledge, making it suitable for scientific applications. However, it often suffers from scalability limitations due to the high computational cost of evaluating and sampling over complex tree structures.

One notable contribution is the Bayesian symbolic regression framework proposed by Jin et al., where trees are constructed from a library of basis functions and scored according to both data fit and model complexity [67]. A Bayesian logic-guided GP variant has also been proposed to embed auxiliary truths and reject expressions inconsistent with physical constraints.

7.2.4 Random Search and Greedy Algorithms

In contrast to GP and SA, random search explores the space of expressions by stochastically generating candidate trees and retaining the best-scoring ones. Surprisingly, studies have shown that random search can match or even outperform GP on certain domains when coupled with effective filtering strategies [68], [69].

Greedy algorithms such as SymTree further refine this idea by incrementally constructing expressions through a deterministic process. Given a predefined grammar (e.g., combinations of polynomials and trigonometric functions), the algorithm expands expressions step-by-step by evaluating local improvements in accuracy and complexity. While fast and interpretable, such methods are typically limited by their rigid structure and inability to escape local optima.

7.3 Problem Formalization and Evaluation Criteria

Symbolic regression involves searching for a function g such that $g \approx f$ and g is simple. Mathematically, the problem can be framed as a multi-objective optimization:

$$\min_{g \in \mathcal{F}} (L(g; X, y), C(g)) \tag{7-1}$$

where:

- L(g; X, y) measures the loss or prediction error, e.g., RMSE or MAE,
- $\mathcal{C}(g)$ quantifies expression complexity, e.g., number of nodes, depth, number of nonlinear operators.

Solutions to this problem are evaluated along two axes:

- Accuracy: How closely the predicted outputs match ground truth. Commonly used metrics include RMSE, R^2 , or normalized error.
- Simplicity: Often measured using handcrafted heuristics such as:
 - Number of operations
 - Tree depth

×)

- Number of variables
- o Operator type weights (e.g., log and exp penalized more than + or
- Expression length in prefix/postfix notation

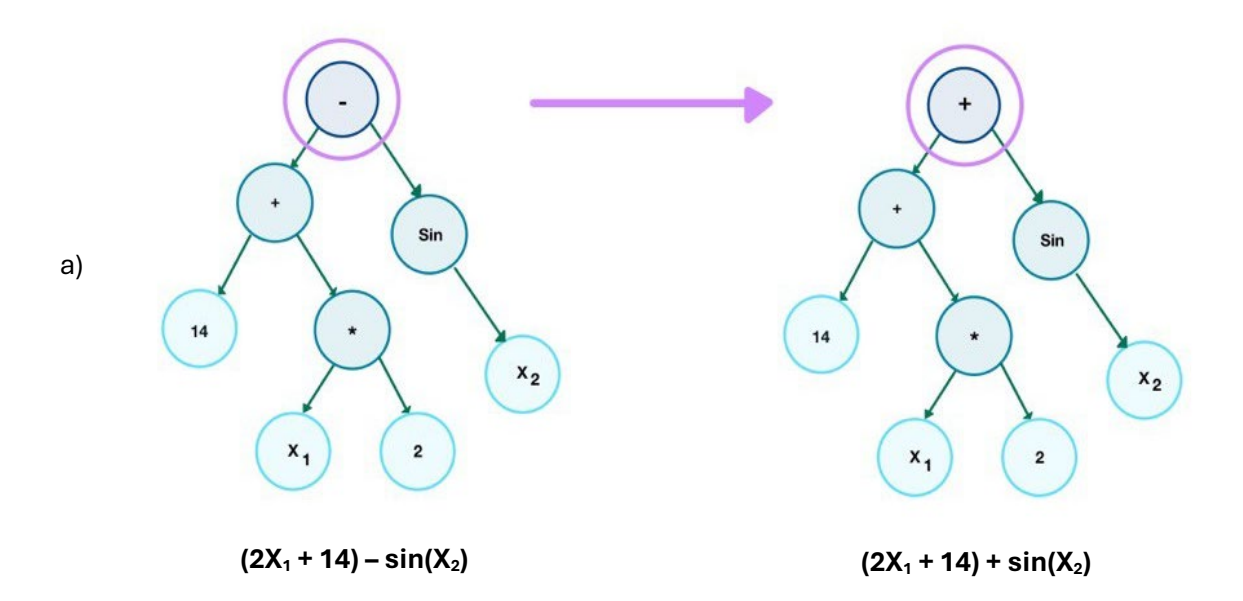
To balance the trade-off between these metrics, the Pareto front is computed. Expressions on this front are non-dominated: no other expression is both more accurate and simpler. Model selection is then guided by the desired trade-off for a specific application, for example maximum interpretability or minimum error.

7.4 Symbolic Regression and PySR

7.4.1 Overview of the PySR Framework

PySR (short for *Python Symbolic Regression*) is a symbolic regression package that combines the expressive power of genetic programming with the efficiency of sparse

optimization and multi-objective search. Developed by Miles Cranmer et al. [70], PySR is implemented in Julia for performance and offers a Python interface for integration with scientific workflows. PySR utilizes a multi-population evolutionary strategy, in which separate "islands" evolve in parallel. Within each island, new individuals (mathematical expressions) are generated via genetic programming operations such as mutation and crossover. The algorithm is inspired by tournament selection, where individuals with lower prediction error and lower complexity are more likely to survive and reproduce [71], [72], while mutation and crossover operations act on symbolic trees to evolve new expressions. These processes are depicted in Figure 7.2.



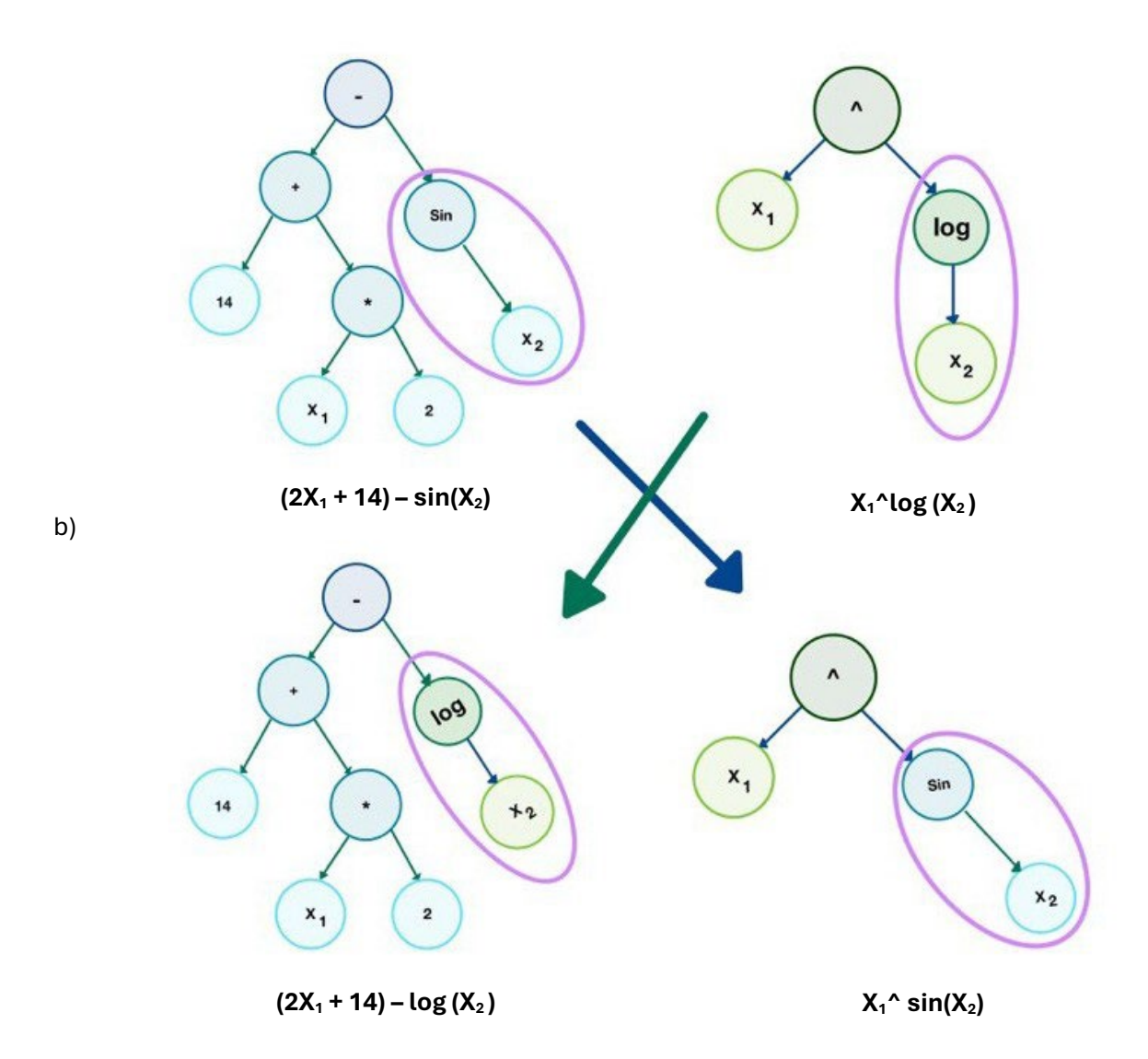


Figure 7.2) a)Mutation applied to the expression tree. b) Crossover applied to two different expression trees

Its core methodology involves evolving populations of candidate mathematical expressions, each composed of user-defined operators (e.g., +, ×, exp, log) and operands (variables and constants), to minimize a loss function based on prediction error. The algorithm maintains a Pareto front of non-dominated expressions that simultaneously optimize for accuracy (e.g., mean squared error) and simplicity (e.g., number of nodes in the expression tree).

Key features of PySR include:

 Multi-objective optimization: Returns a set of expressions balancing complexity and accuracy.

70

Flexible search space: Users can define the allowed operators and

constants.

Fast parallel execution: Uses multi-threading and Just-In-Time (JIT)

compilation via Julia.

Symbolic output: All models are returned as interpretable LaTeX-style

expressions.

A detailed explanation of the algorithm, including design choices and

performance considerations, can be found in the original publication by Miles

Cranmer et al. [70], which describes how symbolic regression is made

computationally tractable through parallelization and optimization of

expression trees.

7.4.2 Configuration and Search Constraints

The symbolic search was configured with strict constraints to control complexity

and ensure interpretability.

Input variables:

Shear rate: $\dot{\gamma}$

Temperature: T (in Kelvin)

Target variable:

Dynamic viscosity: $\eta_{(\dot{v},T)}$ (Pa·s)

Operators allowed:

• {(*, -, +, /, pow)}

Exponential, logarithmic, and nested exponentials were explicitly

disallowed to avoid excessive complexity and improve computational

efficiency.

Loss function:

Mean Squared Error (MSE) between predicted and measured $\log_{10}(\eta)$

Loss =
$$\frac{1}{n} \sum_{i=1}^{n} (\log_{10}(\widehat{\eta_i}) - \log_{10}(\eta_i))^2$$
 (7-2)

Search strategy and complexity control:

- Population size: 500 individuals across 24 subpopulations (island model)
- Maximum generation: 1000
- Dimensional constraint penalty: 10³
- Maximum allowed power in pow(a, b) was constrained to the range $b \in [3,9]$

Pareto optimization:

- Expressions were ranked based on two objectives:
 - 1. Prediction error (MSE)
 - 2. Expression complexity (total number of operations)
- Final selection was made from the Pareto front to ensure a trade-off between accuracy and simplicity.

7.5 Derived MVI Model Expression

The final model selected from the symbolic regression search represents a compact yet powerful expression that implicitly incorporates both shear rate and temperature dependencies. The derived MVI viscosity model is expressed as:

$$\eta(\dot{\gamma}, T) = \frac{(c_1 - T) \cdot c_2}{c_3 + (\dot{\gamma}^2 \cdot (\dot{\gamma} + c_4)^{c_5})}$$
(7-3)

Where:

• c_1 to c_5 are model parameters that must be fitted to experimental data using nonlinear curve fitting techniques such as the bounded Levenberg-Marquardt method implemented via the lmfit library in Python.

Although these parameters are not directly physical constants, they can be interpreted functionally based on their units and behavior as explained in Table 7-1.

Table 7-1) Physical interpretation of MVI model parameters

Parameter	Units	Interpretation
c_1	[K]	Reference temperature used for normalization
c_2	[Pa/(K.s ^(1+C5)]	Thermo-rheological coefficient capturing temperature- shear coupling
c_3	[1/s ^(2+C5)]	Relaxation-related term linked to structural resistance
C_4	[1/s]	Shear rate offset controlling shear-thinning onset
c_5	[-]	Time-scaling exponent affecting nonlinearity of the model

7.5.1 Model Performance

The MVI model showed excellent performance across all datasets tested, achieving a coefficient of determination $R^2>0.95$ even on unseen test and evaluation data, including elastomeric and thermoplastic fluids. The expression consistently preserved physically expected trends:

- Viscosity decreased monotonically with increasing shear rate (shearthinning behavior)
- Viscosity decreased with increasing temperature, consistent with thermal softening

The MVI model achieves full-range coverage, including:

Zero-shear viscosity plateau

- Transition region
- Power-law (pseudoplastic) region

Moreover, the absence of exponential or logarithmic operations significantly improves computational efficiency. On modern CPUs, basic arithmetic operations such as addition, multiplication, and division typically execute in 3–13 cycles, whereas transcendental functions like exp() or log() require 50–200+ cycles due to their computational complexity. By relying solely on algebraic operations, the MVI model minimizes evaluation latency, making it well-suited for embedded implementations within finite-volume solvers or real-time control systems [58].

Finally, the model's smooth, differentiable structure ensures numerical stability when integrated into CFD environments such as OpenFOAM or STAR-CCM+.

Chapter 8 | **Performance and Generalizability**

This chapter evaluates the performance and generalization capability of the proposed Multi-Variable Implicit (MVI) viscosity model. The assessment is carried out in two stages. The first involves a quantitative comparison between the MVI model and established classical viscosity formulations using the designated test dataset. The second stage examines the model's predictive behavior on an independent dataset comprising different polymer materials not included in the training process. These analyses collectively provide insight into the accuracy, robustness, and extrapolation potential of the MVI model across diverse flow and thermal conditions, demonstrating its suitability for practical rheological and CFD applications.

8.1 Test Set Evaluation and Comparison with Classical Models

To begin the evaluation, the MVI model was tested on a dedicated test set composed of data points that were not used during model training. This test set was designed to assess the model's generalization ability to unseen data, and to provide a fair basis for comparison with a classical viscosity model.

For benchmarking purposes, the Carreau–Arrhenius model was independently refitted on the same test set. While this means the Carreau–Arrhenius model had access to the test data during its fitting, the MVI model encountered these points for the first time. Although this creates an uneven comparison, it emphasizes the MVI model's true generalization capability, since it was never optimized on the test data. This comparison serves to evaluate how well the symbolic MVI model can approximate classical rheological behavior on previously unseen data.

Figure 8.1 and Figure 8.2 show the predicted viscosity curves of both models evaluated on the test set. The MVI model achieved a coefficient of determination of $R^2 = 99$, a Bayesian Information Criterion (BIC) value of 1187, and a Root Mean Squared Standardized Residual (RMSSR) of 1.00118. These metrics confirm that the MVI model delivers excellent predictive accuracy while maintaining a compact, closed-form structure optimized for computational efficiency.

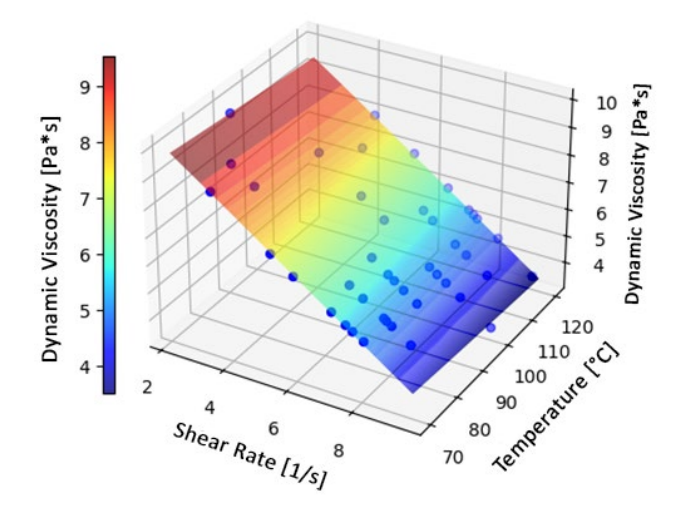


Figure 8.1) Carreau-Arrhenius fit results on the test set

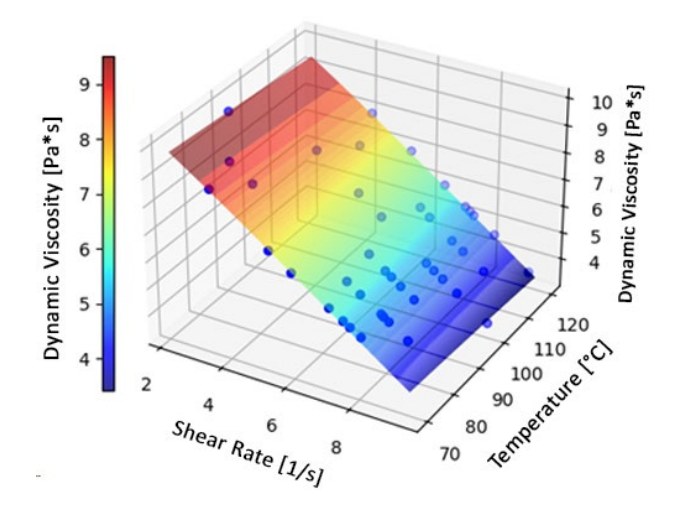


Figure 8.2) MVI Model fit results on the test set

In particular, the MVI model successfully captures the transition from the Newtonian plateau to the pseudoplastic region, and exhibits smooth, stable behavior across the full shear rate spectrum. It also demonstrates strong extrapolation capability in low shear regions, where the accurate representation of zero-shear viscosity is essential for both rheological analysis and CFD applications. These capabilities can be observed in Figure 8.3 and Figure 8.4 where both MVI model and Carreau-Arrhenius model are extrapolated to compare their ability to capture Newtonian plateau and transition region.

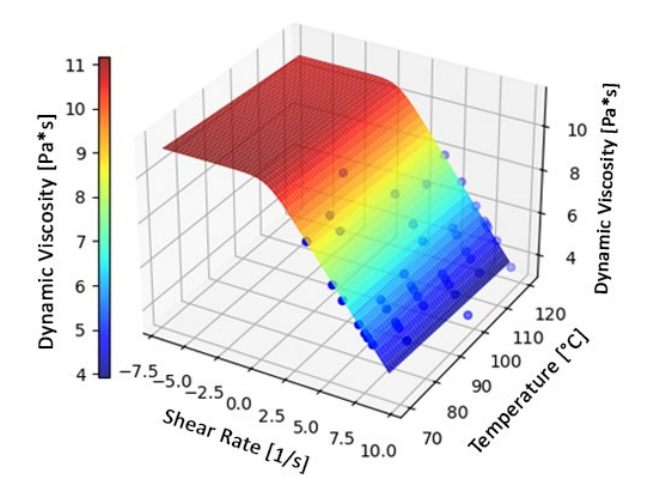


Figure 8.3) Extrapolation of Carreau-Arrhenius model on the test set

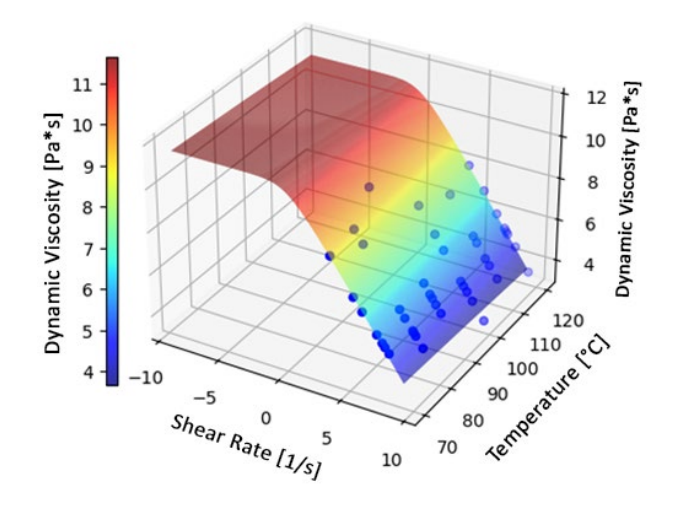
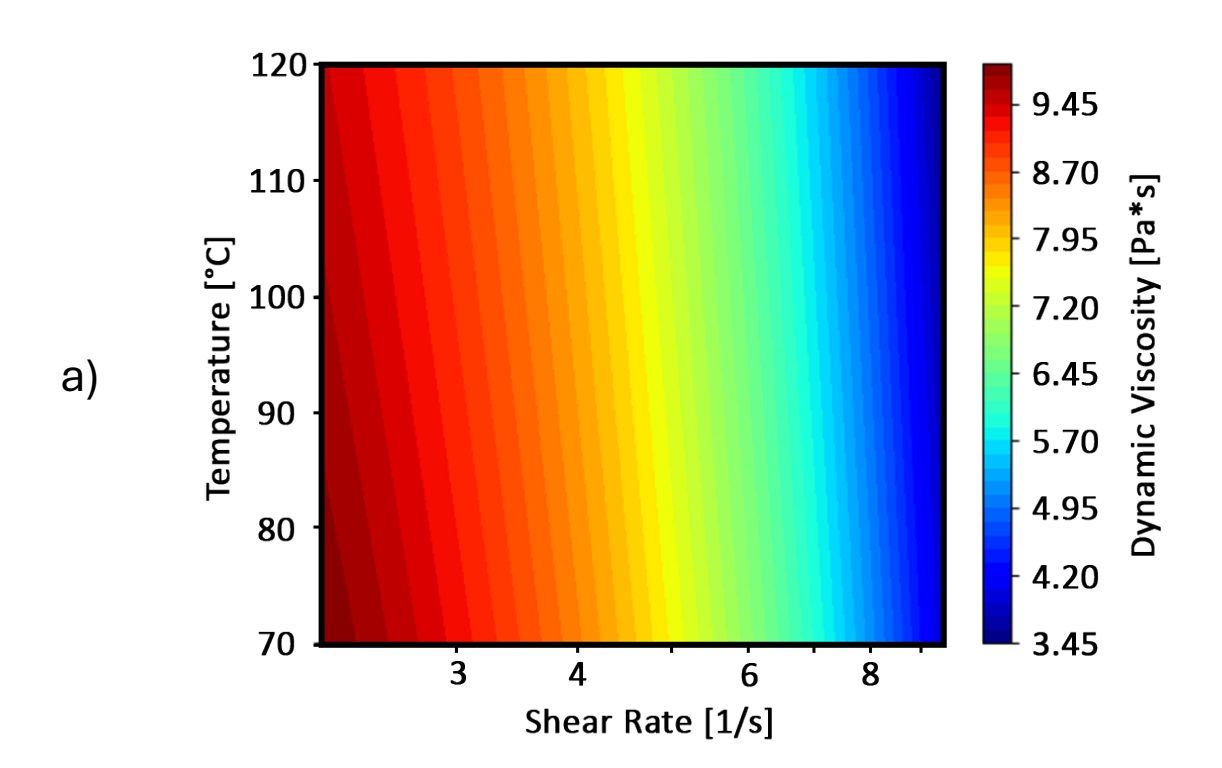


Figure 8.4) Extrapolation of MVI model on the test set

Viscosity contours as a function of shear rate and temperature, presented in Figure 8.5, further confirm the model's physical realism. Notably, Figure 8.6 illustrates the model's ability to reproduce temperature shift behavior, although small deviations are visible in the Newtonian region, which is an acceptable trade-off resulting from symbolic simplification.



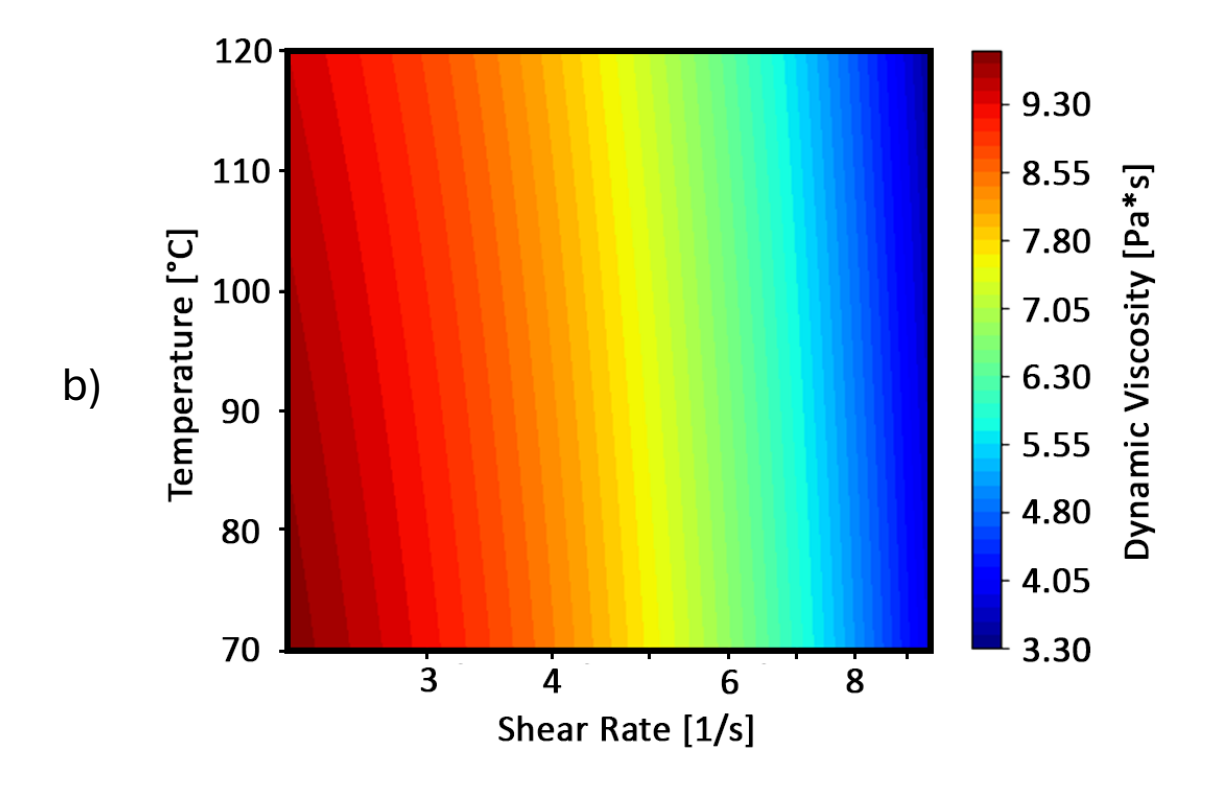


Figure 8.5) a) Carreau-Arrhenius viscosity contour on the test set. b) MVI Viscosity model viscosity contour on the test set.

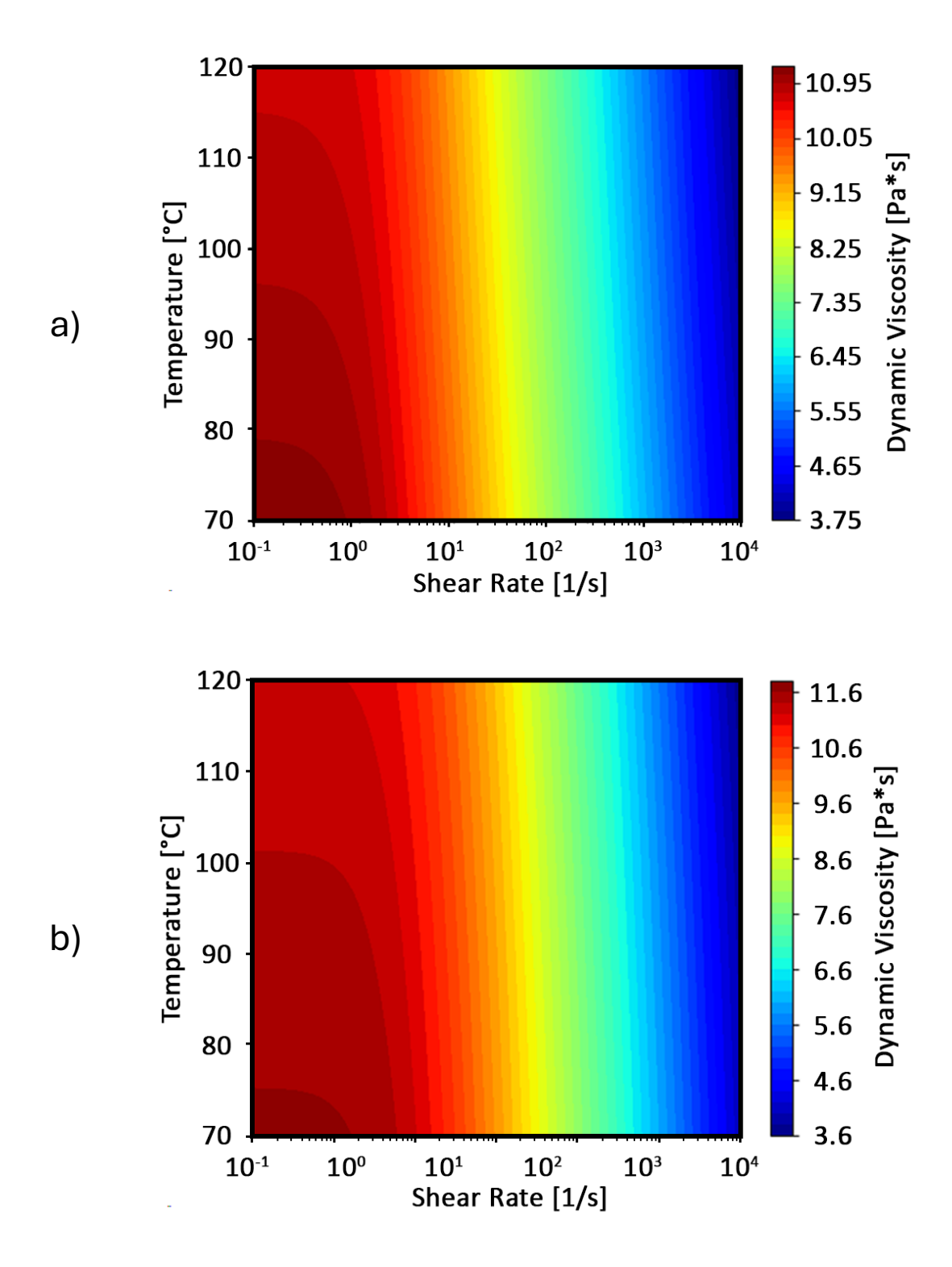


Figure 8.6) a) Carreau-Arrhenius model extrapolation of the viscosity contour on the test set. b) MVI Viscosity model extrapolation of the viscosity contour on the test set.

Table 8-1 and Table 8-2 summarize the fitted parameters for both the MVI and Carreau–Arrhenius models, allowing a direct comparison in terms of parameter scale and functional interpretation.

Table 8-1) Derived variables of Carreau-Arrhenius viscosity model.

Carreau-Arrhenius

n [-]	0.185
E [J/mol]	9484
η_0 [Pa. s]	2592
λ[s]	0.535

Table 8-2) Derived variables of MVI viscosity model.

MVI Viscosity Model

C ₁ [K]	492.12
$C_2[Pa/(K.s^{(1+C_5)}]$	903.5
C ₃ [1/s ^(2+C₅)]	1.19
C ₄ [1/s]	0.525
C ₅ [-]	-1.16

8.2 Evaluation on an Independent Dataset

To evaluate the generalizability of the proposed model, an independent validation study was conducted using three thermoplastic polymers with rheological properties distinct from the elastomer used during model training: polypropylene (PP), polystyrene (PS), and acrylonitrile butadiene styrene (ABS).

The measurements were carried out using an Anton Paar MCR 302 rheometer in parallel-plate mode under a nitrogen atmosphere. Samples were compression molded into disc-shaped specimens with a diameter of 25 mm and a thickness of 1 mm. For each material, frequency-sweep tests were conducted within the linear viscoelastic region across an angular frequency range of 0.1–121 rad/s. The Cox–Merz rule was then applied to convert oscillatory data into steady-shear viscosity data. The viscosity measurement of these 3 datasets at different temperatures are depicted in Figure 8.7.

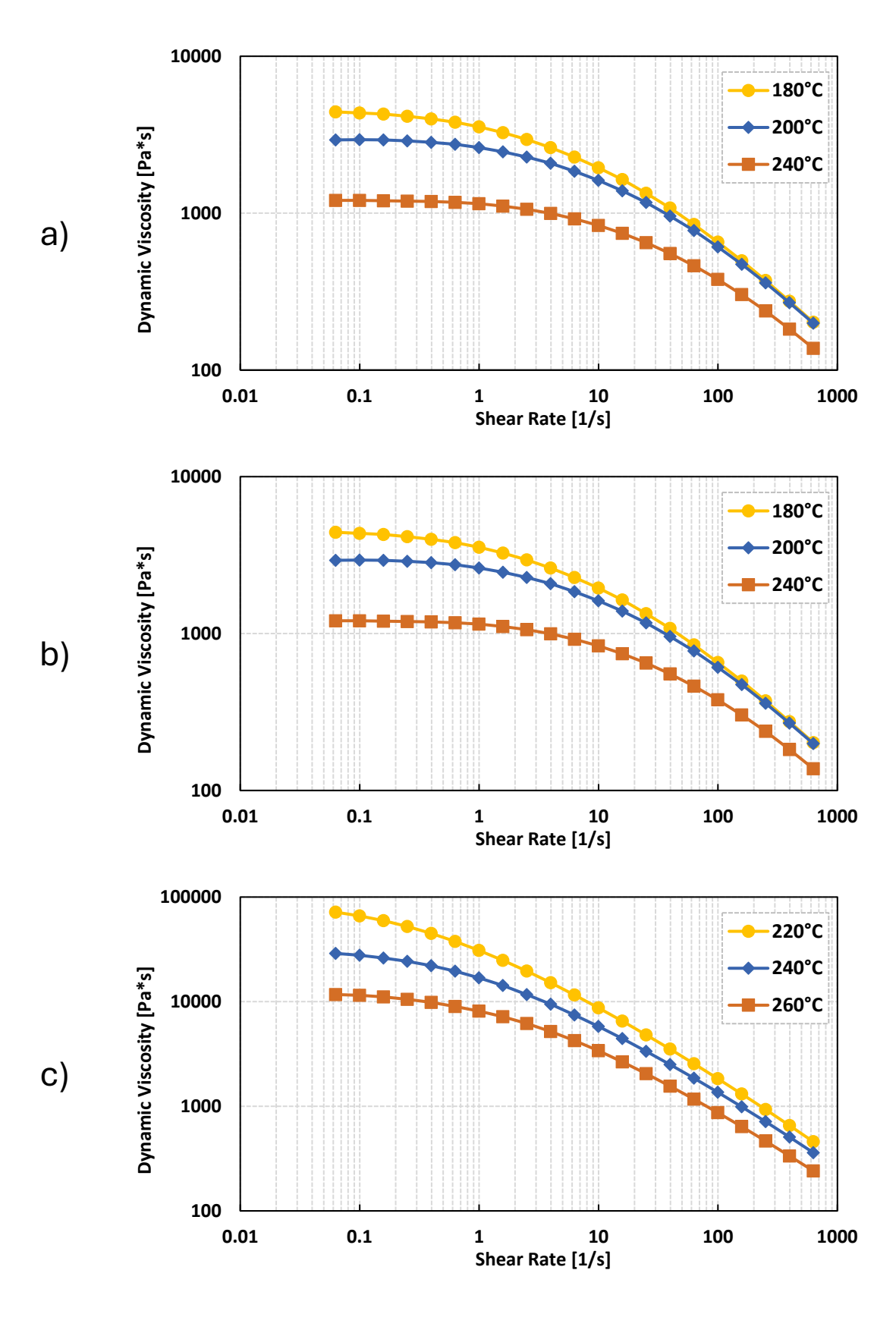
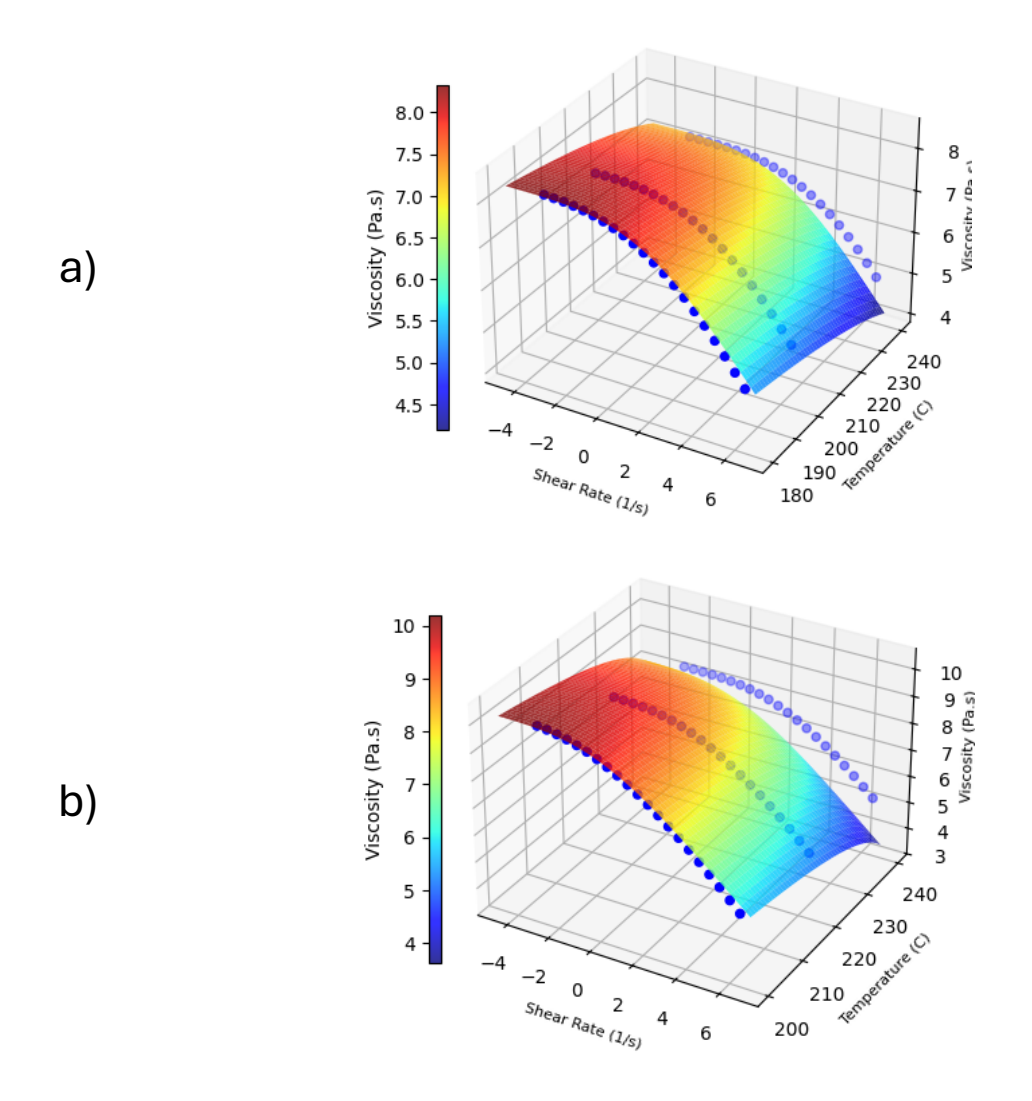


Figure 8.7) Viscosity measurements of independent validation datasets under varying shear rates and temperatures: a) Polypropylene (PP) b) Polystyrene (PS) c)Acrylonitrile Butadiene Styrene (ABS). The plot is in logarithmic scale.

Figure 8.8 presents the fit results of the MVI model for the three independent compounds. Importantly, the model was applied directly without any retraining or parameter tuning, underscoring its flexibility. Across all three polymers, the MVI model accurately captured both shear-thinning behavior and temperature sensitivity, successfully predicting the viscosity trends observed experimentally.



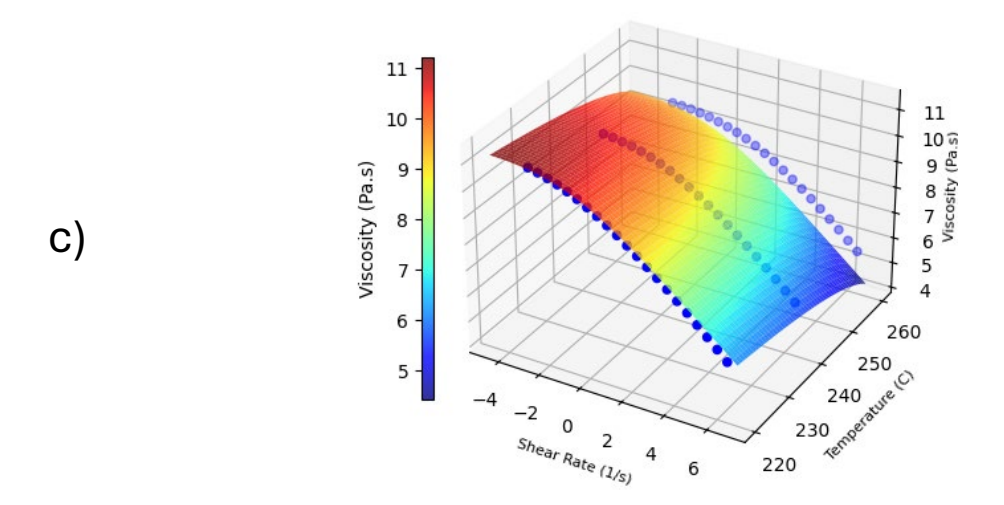


Figure 8.8) Fit results of the MVI viscosity model on independent validation datasets: a)

Polypropylene (PP) b) Polystyrene (PS) c) Acrylonitrile-Butadiene-Styrene (ABS)

To quantify the model's generalization capability, key performance metrics were computed for each material, including:

• R²: Coefficient of determination

BIC: Bayesian Information Criterion

RMSSR: Root Mean Squared Standardized Residual

The results, summarized in Table 8-3, confirm that the MVI model consistently delivers high predictive accuracy across all cases. For each of the three polymer types, the R^2 value remains above 0.95, while **BIC** and **RMSSR** values are within acceptable ranges, reflecting both data conformity and numerical stability.

Table 8-3) Fit statistics of MVI viscosity model un independent dataset.

Material	R ²	BIC	RMSSR
PP	0.990	624.5	1.00629
PS	0.957	938.1	1.00416
ABS	0.977	1005.3	1.00456

These findings validate the model's ability to handle a broad spectrum of non-Newtonian fluids beyond its original training domain. Its closed-form structure, implicit handling of shear rate and temperature effects, and computational simplicity make it particularly suitable for implementation in CFD workflows and engineering simulation tools.

Chapter 9 | **Conclusion and Future Work**

This final chapter summarizes the main outcomes and contributions of the research, providing a synthesis of the modeling framework developed throughout the thesis. The discussion revisits the objectives introduced in Chapter 1 and evaluates how they were achieved through a combination of experimental data analysis, classical rheological modeling, and symbolic regression. The performance and generalization results of the proposed Multi-Variable Implicit (MVI) model are reviewed, followed by a discussion of its limitations and potential directions for future development. Together, these reflections consolidate the scientific and practical significance of the MVI approach in advancing data-driven rheological modeling for computational fluid dynamics applications.

9.1 Conclusion

This thesis introduced a new closed-form Multi-Variable Implicit (MVI) viscosity model capable of accurately representing the shear-thinning and temperature-dependent behavior of non-Newtonian fluids. The model was derived through symbolic regression and trained on a hybrid dataset combining experimentally corrected capillary rheometry measurements and physically consistent synthetic data generated using the Carreau–Arrhenius model.

Unlike classical models that rely on predefined functional forms, the MVI model was discovered purely from data, yet respects physical trends such as:

- decreasing viscosity with increasing shear rate,
- · temperature-induced softening,
- and smooth transition across viscosity regimes.

The final expression is algebraic and compact, using only five parameters, with no exponential or logarithmic terms. This makes it computationally lightweight and CFD-friendly, suitable for integration in simulation environments where efficiency and robustness are critical.

Model performance was validated in two stages:

- A test set consisting of unseen data showed excellent agreement (R² > 0.99),
 confirming the model generalizes well to data it was not trained on.
- An independent dataset of thermoplastic materials demonstrated strong generalizability, confirming the model's versatility across fluid classes.

9.2 Limitations and Future Work

While the MVI model successfully reproduces the zero-shear plateau, transition region, and power-law behavior, it does not capture the second Newtonian plateau that some materials exhibit at very high shear rates. This is a known limitation of the model structure discovered through symbolic regression under the imposed operator constraints and training dataset composition.

Future research can explore:

- Alternative symbolic structures that explicitly allow for multiple plateau behaviors,
- Inclusion of additional data from extreme shear rate regions to guide the model toward second plateau behavior,
- Relaxation of operator constraints (e.g., reintroducing bounded exponential functions) if necessary to improve accuracy in specific regimes.

The approach demonstrated here offers a solid foundation for further model development by combining experimental accuracy, symbolic interpretability, and CFD compatibility. Future work may extend this framework to broader fluid classes, including viscoelastic and shear-thickening materials.

Bibliography

- [1] B. R. Gupta, "Fluid Flow Analysis," in *Rheology Applied in Polymer Processing*, London: CRC Press, 2022, pp. 59–116. doi: 10.1201/9781003344971-3.
- [2] H. Wang, faleh rabhi, A. Cherouat, A. Gilbin, and T. Barriere, "Experimental and numerical investigation of extrudate swell of polylactic acid via Extrusion-based Additive Manufacturing process," Dec. 20, 2022. doi: 10.21203/rs.3.rs-2369014/v1.
- [3] M. Dolz, J. Delegido, A. Casanovas, and a-J. Hern, "A Low-Cost Experiment on Newtonian and Non-Newtonian Fluids," 2005. [Online]. Available: www.JCE.DivCHED.org
- [4] R. P. Chhabra and J. F. Richardson, "Non-Newtonian Fluid Behaviour," in *Non-Newtonian Flow and Applied Rheology*, Elsevier, 2008, pp. 1–55. doi: 10.1016/B978-0-7506-8532-0.00001-9.
- [5] M. Hassan, A. Faisal, K. Javid, S. Khan, A. Ahmad, and R. Khan, "The Impact of Different Arrangements of Molecular Chains in Terms of Low and High Shear Rate's Viscosities on Heat and Mass Flow of Nonnewtonian Shear thinning Fluids," Comb Chem High Throughput Screen, vol. 25, no. 7, pp. 1115–1126, Jul. 2022, doi: 10.2174/1386207324666210719111909.
- [6] M. S. Salehi, M. T. Esfidani, H. Afshin, and B. Firoozabadi, "Experimental investigation and comparison of Newtonian and non-Newtonian shear-thinning drop formation," *Exp Therm Fluid Sci*, vol. 94, pp. 148–158, Jun. 2018, doi: 10.1016/j.expthermflusci.2018.02.006.
- [7] S. Azeez and V. Bertola, "Lubrication of journal bearings by shear thinning lubricants using different constitutive models," *Proceedings of the Institution of Mechanical Engineers, Part J: Journal of Engineering Tribology*, vol. 235, no. 6, pp. 1203–1210, Jun. 2021, doi: 10.1177/1350650120950521.
- [8] M. Wrobel, "On the application of simplified rheological models of fluid in the hydraulic fracture problems," *Int J Eng Sci*, vol. 150, May 2020, doi: 10.1016/j.ijengsci.2020.103275.

- [9] V. S. Tanmay, R. Patne, and V. Shankar, "Stability of plane Couette flow of Carreau fluids past a deformable solid at arbitrary Reynolds numbers," *Physics of Fluids*, vol. 30, no. 7, Jul. 2018, doi: 10.1063/1.5041771.
- [10] H. E. Fayed, N. A. Sheikh, and O. Iliev, "On Laminar Flow of Non-Newtonian Fluids in Porous Media," *Transp Porous Media*, vol. 111, no. 1, pp. 253–264, Jan. 2016, doi: 10.1007/s11242-015-0592-8.
- [11] S. Karimi, M. Dabagh, P. Vasava, M. Dadvar, B. Dabir, and P. Jalali, "Effect of rheological models on the hemodynamics within human aorta: CFD study on CT image-based geometry," *J Nonnewton Fluid Mech*, vol. 207, pp. 42–52, 2014, doi: 10.1016/j.jnnfm.2014.03.007.
- [12] S. Bair, "Generalized Newtonian viscosity functions for hydrodynamic lubrication," *Tribol Int*, vol. 117, pp. 15–23, Jan. 2018, doi: 10.1016/j.triboint.2017.08.014.
- [13] C. Marschik, W. Roland, B. Löw-Baselli, and J. Miethlinger, "A heuristic method for modeling three-dimensional non-Newtonian flows of polymer melts in single-screw extruders," Oct. 01, 2017, *Elsevier B.V.* doi: 10.1016/j.jnnfm.2017.08.007.
- [14] K. J. Ruschak and S. J. Weinstein, "A local power-law approximation to a smooth viscosity curve with application to flow in conduits and coating dies," Polym Eng Sci, vol. 54, no. 10, pp. 2301–2309, Oct. 2014, doi: 10.1002/pen.23782.
- [15] J. Gołdasz and B. Sapiński, "CFD Study of the Flow of MR Fluids," in *Insight into Magnetorheological Shock Absorbers*, Cham: Springer International Publishing, 2015, pp. 117–130. doi: 10.1007/978-3-319-13233-4_6.
- [16] V. A. Popova and N. V. Surovtsev, "Transition from Arrhenius to non-Arrhenius temperature dependence of structural relaxation time in glass-forming liquids: Continuous versus discontinuous scenario," *Phys Rev E*, vol. 90, no. 3, p. 032308, Sep. 2014, doi: 10.1103/PhysRevE.90.032308.

- [17] M. P. Recondo, B. E. Elizalde, and M. P. Buera, "Modeling temperature dependence of honey viscosity and of related supersaturated model carbohydrate systems," *J Food Eng*, vol. 77, no. 1, pp. 126–134, Nov. 2006, doi: 10.1016/j.jfoodeng.2005.06.054.
- [18] D. R. Cassar, "ViscNet: Neural network for predicting the fragility index and the temperature-dependency of viscosity," *Acta Mater*, vol. 206, p. 116602, Mar. 2021, doi: 10.1016/j.actamat.2020.116602.
- [19] D. Li, X. Zhang, and Q. Kang, "Machine learning estimation of crude oil viscosity as function of API, temperature, and oil composition: Model optimization and design space," *PLoS One*, vol. 18, no. 2, p. e0282084, Feb. 2023, doi: 10.1371/journal.pone.0282084.
- [20] A. M. Elsharkwy and R. B. C. Gharbi, "Comparing classical and neural regression techniques in modeling crude oil viscosity." [Online]. Available: www.elsevier.com/locate/advengsoft
- [21] M. A. Ayoub, D. M. Raja, and M. A. Al-Marhoun, "Evaluation of Below Bubble Point Viscosity Correlations & Construction of a New Neural Network Model," in Asia Pacific Oil and Gas Conference and Exhibition, SPE, Oct. 2007. doi: 10.2118/108439-MS.
- [22] Y. Hajizadeh, "Intelligent Prediction of Reservoir Fluid Viscosity," in *Production and Operations Symposium*, SPE, Mar. 2007. doi: 10.2118/106764-MS.
- [23] M. Saadat, M. Mahmoudabadbozchelou, and S. Jamali, "Data-driven selection of constitutive models via rheology-informed neural networks (RhINNs)," *Rheol Acta*, vol. 61, no. 10, pp. 721–732, Oct. 2022, doi: 10.1007/s00397-022-01357-w.
- [24] F. Irgens, *Rheology and Non-Newtonian Fluids*. Cham: Springer International Publishing, 2014. doi: 10.1007/978-3-319-01053-3.
- [25] M. R. Kamal and H. Nyun, "The Effect of Pressure on the Shear Viscosity of Polymer Melts," *Transactions of the Society of Rheology*, vol. 17, no. 2, pp. 271–285, Jul. 1973, doi: 10.1122/1.549315.

- [26] H. M. Laun, "Capillary rheometry for polymer melts revisited," *Rheol Acta*, vol. 43, no. 5, pp. 509–528, Nov. 2004, doi: 10.1007/s00397-004-0387-2.
- [27] K. WALTERS, "Oscillatory Experiments with a Cone-and-plate Viscometer," *Nature*, vol. 200, no. 4905, pp. 458–458, Nov. 1963, doi: 10.1038/200458a0.
- [28] C. Kukla, I. Duretek, J. Gonzalez-Gutierrez, and C. Holzer, "Rheology of PIM feedstocks," *Metal Powder Report*, vol. 72, no. 1, pp. 39–44, Jan. 2017, doi: 10.1016/j.mprp.2016.03.003.
- [29] L. Lang, S. Alexandrov, E. Lyamina, and V. M. Dinh, "The Behavior of Melts with Vanishing Viscosity in the Cone-and-Plate Rheometer," *Applied Sciences*, vol. 10, no. 1, p. 172, Dec. 2019, doi: 10.3390/app10010172.
- [30] J. Mewis and N. J. Wagner, *Colloidal Suspension Rheology*. Cambridge University Press, 2011. doi: 10.1017/CBO9780511977978.
- [31] S. Syrjälä and J. Aho, "Capillary rheometry of polymer melts Simulation and experiment," *Korea-Australia Rheology Journal*, vol. 24, no. 3, pp. 241–247, Sep. 2012, doi: 10.1007/s13367-012-0029-7.
- [32] H. R. Juster, T. Distlbacher, and G. Steinbichler, "Viscosity Analysis of a Polymer-Based Drug Delivery System Using Open-Source CFD Methods and High-Pressure Capillary Rheometry," *International Polymer Processing*, vol. 29, no. 5, pp. 570–578, Nov. 2014, doi: 10.3139/217.2892.
- [33] I. Duretek, S. Schuschnigg, A. Gooneie, G. R. Langecker, and C. Holzer, "Rheological properties of wood polymer composites and their role in extrusion," *J Phys Conf Ser*, vol. 602, p. 012014, Apr. 2015, doi: 10.1088/1742-6596/602/1/012014.
- [34] C. Kukla, I. Duretek, J. Gonzalez-Gutierrez, and C. Holzer, "Rheology of Highly Filled Polymers," in *Polymer Rheology*, InTech, 2018. doi: 10.5772/intechopen.75656.
- [35] C. Hopmann and W. Michaeli, Extrusion Dies for Plastics and Rubber. München: Carl Hanser Verlag GmbH & Co. KG, 2016. doi: 10.3139/9781569906248.

- [36] E. B. Bagley, "End Corrections in the Capillary Flow of Polyethylene," *J Appl Phys*, vol. 28, no. 5, pp. 624–627, May 1957, doi: 10.1063/1.1722814.
- [37] J. Aho and S. Syrjälä, "Evaluation of Different Methods for Determining the Entrance Pressure Drop in Capillary Rheometry," *Applied Rheology*, vol. 18, no. 6, pp. 63258-1-63258–5, Dec. 2008, doi: 10.1515/arh-2008-0022.
- [38] H. M. Laun, "Capillary rheometry for polymer melts revisited," *Rheol Acta*, vol. 43, no. 5, pp. 509–528, Nov. 2004, doi: 10.1007/s00397-004-0387-2.
- [39] B. Rabinowitsch, "Über die Viskosität und Elastizität von Solen."
- [40] S. Syrjälä and J. Aho, "Capillary rheometry of polymer melts Simulation and experiment," *Korea-Australia Rheology Journal*, vol. 24, no. 3, pp. 241–247, Sep. 2012, doi: 10.1007/s13367-012-0029-7.
- [41] "ISO. Plastics-Determination of the Fluidity of Plastics Using Capillary and Slit-Die Rheometers; ISO: Geneva, Switzerland, 2021; p. 11443.".
- [42] A. Sorrentino and R. Pantani, "Determination of the effect of pressure on viscosity of an isotactic polypropylene," *Polymer Bulletin*, vol. 70, no. 7, pp. 2005–2014, Jul. 2013, doi: 10.1007/s00289-013-0913-4.
- [43] J. H. PRENTICE, "Dimensional Problem of the Power Law in Rheology," *Nature*, vol. 217, no. 5124, pp. 157–157, Jan. 1968, doi: 10.1038/217157a0.
- [44] P. J. Carreau, "Rheological Equations from Molecular Network Theories," *Transactions of the Society of Rheology*, vol. 16, no. 1, pp. 99–127, Mar. 1972,
 doi: 10.1122/1.549276.
- [45] Kenji. Yasuda, "INVESTIGATION OF THE ANALOGIES BETWEEN." [Online].

 Available: http://libraries.mit.edu/ask
- [46] S. Karimi, M. Dabagh, P. Vasava, M. Dadvar, B. Dabir, and P. Jalali, "Effect of rheological models on the hemodynamics within human aorta: CFD study on CT image-based geometry," *J Nonnewton Fluid Mech*, vol. 207, pp. 42–52, May 2014, doi: 10.1016/j.jnnfm.2014.03.007.

- [47] S.-Y. Kim and S.-H. Park, "Identification of Cross-WLF Viscosity Model Parameters Using Optimization Technique 최적화기법을 이용한 Cross-WLF점도 모델 계수 추정," Journal of the Korea Academia-Industrial cooperation Society, vol. 19, no. 4, pp. 623–632, 2018, doi: 10.5762/KAIS.2018.19.4.623.
- [48] Dino Ferri, Andrea Perolo, and Mirco Nodari, "Cross-WLF parameters to predict rheological properties of polylactic acid".
- [49] J. Tian and L. Zhang, "Contribution to modeling the viscosity Arrhenius-type equation for saturated pure fluids," *Int J Mod Phys B*, vol. 30, no. 27, p. 1650202, Oct. 2016, doi: 10.1142/S0217979216502027.
- [50] A. C. P. Rosa, P. Vaveliuk, K. C. Mundim, and M. A. Moret, "A model for diffusive systems: Beyond the Arrhenius mechanism," *Physica A: Statistical Mechanics and its Applications*, vol. 450, pp. 317–322, May 2016, doi: 10.1016/j.physa.2015.12.122.
- [51] L. Dagdug and L. S. García-Colín, "Generalization of the stochastic matrix method and theoretical framework for the VFT equation in strong glasses," *Journal of Physics: Condensed Matter*, vol. 11, no. 24, pp. 4575–4582, Jun. 1999, doi: 10.1088/0953-8984/11/24/301.
- [52] M. L. Williams, R. F. Landel, and J. D. Ferry, "Temperature Dependence of Relaxation Mechanisms The Temperature Dependence of Relaxation Mechanisms in Amorphous Polymers and Other Glass-forming Liquids1," 1955.
- [53] "Appendix 1: The Williams Landau Ferry (WLF) Equation and Time Temperature Superposition," in *Principles and Applications of Thermal Analysis*, Wiley, 2008, pp. 450–452. doi: 10.1002/9780470697702.app1.
- [54] P. A. Tanguy, L. Choplin, and P. Hurez, "Compensation Effects in Viscosity-Temperature Dependence of Polymer Melts."
- [55] N. M. Rudolph, A. C. Agudelo, J. C. Granada, H. E. Park, and T. A. Osswald, "WLF model for the pressure dependence of zero shear viscosity of

- polycarbonate," *Rheol Acta*, vol. 55, no. 8, pp. 673–681, Aug. 2016, doi: 10.1007/s00397-016-0945-4.
- [56] B. Aşikgil, "Robust Nonlinear Least Squares Approaches for Evaluating OVA-Mediated Bleaching Reactions: An Experimental Comparative Study." [Online]. Available: http://dergipark.gov.tr/gujs
- [57] "M. Newville et al., lmfit: Non-linear optimization and curve fitting, 2024. [Online]. Available: https://lmfit.github.io/lmfit-py/".
- [58] A. Gholamy, V. Kreinovich, and O. Kosheleva, "Why 70/30 or 80/20 Relation Between Training and Testing Sets: A Pedagogical Explanation," https://api.semanticscholar.org/CorpusID:7467506.
- [59] J. Hou, X. Chen, T. Wu, E. Kuhl, and X. Wang, "Automated data-driven discovery of material models based on symbolic regression: A case study on the human brain cortex," *Acta Biomater*, vol. 188, pp. 276–296, Oct. 2024, doi: 10.1016/j.actbio.2024.09.005.
- [60] J. R. Koza, "Genetic programming as a means for programming computers by natural selection," 1994.
- [61] D. Angelis, F. Sofos, and T. E. Karakasidis, "Artificial Intelligence in Physical Sciences: Symbolic Regression Trends and Perspectives," *Archives of Computational Methods in Engineering*, vol. 30, no. 6, pp. 3845–3865, Jul. 2023, doi: 10.1007/s11831-023-09922-z.
- [62] P. Dominic, D. Leahy, and M. Willis, GPTIPS: An Open Source Genetic Programming Toolbox For Multigene Symbolic Regression, vol. 2180. Lecture Notes in Engineering and Computer Science, 2010.
- [63] S.-M. Udrescu and M. Tegmark, "AI Feynman: A physics-inspired method for symbolic regression," 2020. [Online]. Available: http://advances.sciencemag.org/
- [64] M. Schmidt and H. Lipson, "Distilling Free-Form Natural Laws from Experimental Data," Science (1979), vol. 324, no. 5923, pp. 81–85, Apr. 2009, doi: 10.1126/science.1165893.

- [65] B. Burlacu, G. Kronberger, and M. Kommenda, "Operon C++," in *Proceedings of the 2020 Genetic and Evolutionary Computation Conference Companion*, New York, NY, USA: ACM, Jul. 2020, pp. 1562–1570. doi: 10.1145/3377929.3398099.
- [66] S. Becker, "'gplearn: Genetic Programming in Python,' [Online]. Available: https://github.com/trevorstephens/gplearn. Accessed: Jul. 2025."
- [67] Y. Jin, W. Fu, J. Kang, J. Guo, and J. Guo, "Bayesian Symbolic Regression," Jan. 2020, [Online]. Available: http://arxiv.org/abs/1910.08892
- [68] Y. Qi, X. Mao, Y. Lei, Z. Dai, and C. Wang, "The strength of random search on automated program repair," in *Proceedings of the 36th International Conference on Software Engineering*, New York, NY, USA: ACM, May 2014, pp. 254–265. doi: 10.1145/2568225.2568254.
- [69] J. Bergstra, J. B. Ca, and Y. B. Ca, "Random Search for Hyper-Parameter Optimization Yoshua Bengio," 2012. [Online]. Available: http://scikit-learn.sourceforge.net.
- [70] M. Cranmer, "Interpretable Machine Learning for Science with PySR and SymbolicRegression.jl," May 2023, [Online]. Available: http://arxiv.org/abs/2305.01582
- [71] "Anne Brindle. Genetic Algorithms for Function".
- [72] D. E. Goldberg and K. Deb, "A Comparative Analysis of Selection Schemes Used in Genetic Algorithms."